Advancements in multi-rupture time-dependent seismic hazard modeling, including fault interaction

Salvatore Iacoletti[(1)], Gemma Cremen[(2)], Carmine Galasso[(3)]

(1) PhD Student, Department of Civil, Environmental and Geomatic Engineering, University College London, UK, salvatore.iacoletti.19@ucl.ac.uk

(2) Research Fellow, Department of Civil, Environmental and Geomatic Engineering, University College London, UK, g.cremen@ucl.ac.uk

(3) Associate Professor, Department of Civil, Environmental and Geomatic Engineering, University College of London, UK, and Scuola Universitaria Superiore (IUSS) Pavia, Italy, c.galasso@ucl.ac.uk

1 Introduction

Probabilistic seismic hazard analysis (PSHA) for a specific site provides the rate at which an earthquake-induced ground-motion intensity measure (IM) (e.g., peak accelerations) exceeds a pre-defined threshold during a specified time window (McGuire 2004). PSHA includes two main subcomponents (Field et al. 2003): (1) an earthquake rupture forecast (ERF), which specifies the probability of occurrence of different earthquake ruptures (i.e., different magnitudes, locations, and faulting types) for each seismic source in a region, over a given period; and (2) a ground-motion model (GMM), which determines the probability distribution of various IMs at the site, given the occurrence of a specified earthquake rupture (i.e., an earthquake of a certain magnitude occurring at a nearby location). PSHA uncertainties are categorized as either aleatoric or epistemic (McGuire 2004). Aleatoric variability is the inherent (irreducible) variability in a phenomenon that is captured by modeling the relevant variables in the problem as random variables. Epistemic uncertainty is the modeling uncertainty due to limited data and knowledge. Epistemic uncertainties in PSHA are typically accounted for using logic trees (e.g., Bommer and Scherbaum 2008, Kulkarni et al. 1984). In a logic-tree approach, a single hazard analysis, corresponding to an individual branch of the logic tree, quantifies all aleatoric aspects of the corresponding model. In contrast, the spread of hazard curves for different branches describes the epistemic uncertainty (Bommer and Scherbaum 2008). An expert or an expert group devises a weighted sampling scheme to represent the degree-of-belief in each branch.

An ERF can be developed by (1) identifying all earthquake sources capable of producing damaging ground-motions; (2) defining the characteristics of the sources (e.g., geometry and focal mechanisms) associated with potential earthquakes; and (3) characterizing the distribution of rupture magnitudes and their probability of occurrence for each source (Field et al. 2003, Baker 2015). This study primarily focuses on the ERF component of fault-based PSHA, i.e., fault-based ERF (e.g., Stirling et al. 2012, Demircioğlu et al. 2018).

The general approaches to assemble a fault-based ERF (e.g., Stirling et al. 2012, Field et al. 2009) found in the literature usually comprise the following steps:

1. Identify the fault structures and the corresponding segment boundaries (based on geologic evidence), where each segment potentially represents the extent of a single rupture (i.e., assumed fault segmentation);
2. Identify the long-term rate for every single fault or possible multi-segment rupture (i.e., ruptures, including several fault segments) using geologic slip rate data and paleoseismic studies. Fault slip rates can be derived from measured geologic offsets or estimated by modeling geodetic measurements. Paleoseismic studies usually apply geologic, structural, and chronologic methods to trench-scale deformations and discontinuities to determine probabilistic distributions of the date of past events in a single location (i.e., the trench) and corresponding estimates of fault slip (i.e., displacement);
3. Calibrate the earthquake occurrence model of the faults.

This general approach has several shortcomings. The segmentation hypothesis (point 1) may be inaccurate if physical/geological barriers between fault segments are assumed where they do not exist. Recent events (e.g., 2002 moment magnitude, M_W, 7.9 Denali, USA; 2008 M_W 8.0 Wenchuan, China; 2016 M_W 7.8 Kaikōura earthquake, New Zealand) show that large earthquakes often involve other fault segments in combination with major faults. There is no robust and standardized methodology for defining the long-term occurrence rates (points 2), especially for multi-segment ruptures. This leads to subjectively assigned rate values that are not always reproducible.

The earthquake occurrence model of seismic sources (point 3) is typically represented as a homogeneous Poisson (time-independent) process, which assumes that inter-arrival times between events are independent, identically distributed exponential random variables (i.e., there is no memory of past earthquakes). However, time-independent approaches do not adequately model:

- the long-term time-dependency of mainshocks on specific fault segments, i.e., some evidence suggests that soon after a segment-rupturing earthquake, the probability of having a similar magnitude earthquake might be lower than average (Cornell and Winterstein, 1988);
- the interaction between adjacent faults, i.e., the fact that an earthquake on one fault can result in a tectonic loading change in the surrounding faults, which may delay or promote (i.e., "trigger") the rupture occurrence of other events on those faults (Stein et al. 1997);
- the spatial and temporal clustering of foreshocks and aftershocks (i.e. smaller earthquakes preceding and following the mainshock, respectively), which can have a significant effect on the short-term hazard (Papadopoulos et al. 2020).

The first limitation emphasizes the need to consider time-dependent occurrence models in seismic hazard and loss assessments (Field et al. 2015; Mitchell-Wallace 2017). Besides, there is considerable evidence of interaction between adjacent faults (Stein et al. 1997); this phenomenon is responsible for the occurrence of the Duzce (Turkey) North Anatolian earthquake after the 1999 M_W 7.4 Izmit event, as well all triggered events on the North Anatolian fault in the previous century (Stein et al. 1997, Parsons et al. 2000). Thus, not including fault interaction may produce biased hazard estimates. In addition, most PSHA studies account only for mainshock events. However, recent disasters (e.g., 2010–2011 Christchurch sequence, New Zealand) have highlighted the potential pitfalls of neglecting the effects of aftershocks on the short-term hazard and the need for more advanced tools to overcome the homogeneous Poisson (time-independent) assumption (Papadopoulos et al. 2020).

Recent studies and advances in each of the limitations discussed above tend to focus on one specific aspect in isolation (e.g., Abaimov et al. 2008) and have not investigated how different modeling choices (e.g., segmented vs. unsegmented fault model, time-independent vs. time-dependent occurrence model) interact with each other and affect the PSHA outputs.

The study presented in this paper has two main aims. The first is to review the current literature on fault segmentation and multi-segment ruptures, time-dependent occurrence models and their implementation, and fault interaction effects between subsequent events. In particular, the relation between these three topics will be investigated and critically discussed. The study's second and foremost aim is to develop an advanced, harmonized framework for state-of-the-art fault-based seismic hazard modeling, attempting to address the shortcomings of fault-based ERF for mainshocks (i.e., the first and second limitations mentioned above).

The paper is organized as follows. Section 2 presents a literature review on fault segmentation and multi-segment ruptures, fault interaction effects between subsequent events, time-dependent occurrence models, and their implementation. Section 3 presents the proposed harmonized methodology. Section 4 demonstrates a case study application of the methodology to Wellington city (New Zealand). Section 5 and 6 provide discussion and conclusions, respectively.

2 Literature Review

This section presents a literature review of three main ERF-related aspects of fault-based PSHA, namely fault segmentation and multi-segment rupture, rupture occurrence modeling, and fault interaction.

2.1 Fault segmentation and multi-segment ruptures

One of the first steps of fault-based PSHA is the collection of geologic information to identify potentially active faults and possibly infer the magnitude range of the earthquakes (or ruptures) those faults can generate. The typical segmentation process starts by identifying major fault structures (as opposed to minor fault structures, which are often neglected) that are reasonably continuous at depth for several kilometers. The segment boundaries (i.e., persistent barriers to ruptures) of the fault structures are usually identified according to some geologic criteria such as gaps, sharp bends, or stepovers between faults (Boncio et al.

2004). Note that for the purposes of this study, a "fault" represents a geological feature that poses a potential hazard for the considered study area and "fault segments" represent individual seismic sources within a fault that collectively contribute to the hazard. The geometry of fault segments is usually simplified with respect to the mapped geometry. However, it maintains reasonable consistency with observable features (e.g., the rake of the fault, along-strike length at the surface) of the original fault. These simplified fault segments are directly used for PSHA studies at a regional scale, assuming that the true source inclination and geometry do not significantly affect the ground-shaking response (Boncio et al. 2004, Faure Walker et al 2019).

The fault source model resulting from the segmentation process is typically included in PSHA using the seismic moment balancing approach (e.g., Stirling et al. 2012, Demircioğlu et al. 2018, Field et al. 2009), which assumes that the seismic moment released by an earthquake is related to the strain accumulation along a fault segment during a recurrence interval. The seismic moment calculated for each fault segment can be used to compute the magnitude (or area) of the possible ruptures based on a selected magnitude-frequency distribution (MFD) and the assumptions regarding possible connections between fault segments (e.g., Murru et al. 2016). The choice of MFD affects the type of ruptures considered in fault-based ERF. Assuming a characteristic magnitude model for each fault segment (e.g., Stirling et al. 2012) implies that (1) fault segments are treated as independent seismic sources (Boncio et al. 2004, Pace et al. 2016); and (2) approximately the entire segment surface ruptures for every earthquake (Stirling et al. 2012, Schwartz and Coppersmith, 1984, Boncio et al. 2004). Considering a Gutenberg-Richter MFD (e.g., Demircioğlu et al. 2018) or a mixture of MFD models (e.g., Field et al. 2014) facilitates the occurrence of rupture areas that are smaller than the whole segment surface. These ruptures are often referred to as "floating ruptures" (Visini et al. 2020, Parsons and Geist 2009). Note that assuming a Gutenberg-Richter MFD still results in the treatment of fault segments as independent seismic sources.

Strict fault segmentation models (i.e., where fault segments are independent) may not be adequate for evaluating the potential hazard from medium-to-large magnitude events (dePolo et al. 1991, Schwartz et al. 2012). In fact, geologic evidence shows that historical barriers to rupture may not be persistent (Iezzi et al. 2019), and that earthquakes can "jump" from one fault to another within the fault system. Figure 1 shows the approximate geometry of the 2016 M_W 7.8 Kaikōura (New Zealand) earthquake (Hamling et al. 2017), which involves more than one fault segment (i.e., a multi-segment rupture, also referred to in the literature as "multi-fault" rupture or "multi rupture"). This type of multi-segment rupture would not be captured by a fault-based PSHA that limits ruptures to independent segments. Other examples of multi-segment ruptures are the 1932 M_W 7.2 Cedar Mountain (USA) earthquake (Bell et al. 1999), the 1980 M_W 6.9 Irpinia (Italy) earthquake (Bernard and Zollo, 1989), the 2002 M_W 7.9 Denali fault (USA) earthquake (Eberhart-Phillips et al. 2003, Schwartz et al. 2012), and the 2016 M_W 6.5 Norcia (Italy) earthquake (Villani et al. 2018). However, multi-segment ruptures are typically excluded from fault models (e.g., Stirling et al. 2012, Demircioğlu et al. 2018). Multi-segment ruptures occur when dynamic/static stress changes caused by coseismic slip on one fault segment (or small portions of it) lead to additional rupture propagation on more segments (Harris and Day 1993, Mignan et al. 2015). This process is (almost) instantaneous and leads to larger magnitude earthquakes (i.e., "inter-fault multi-rupture" mentioned in Section 2.3). A simple approach to generate multi-segment ruptures is to assume that some long neighboring segments may rupture together during an earthquake (e.g., Murru et al. 2016, Parsons and Geist 2009). However, it is often impossible to identify all the rupture patterns for a given fault system because of difficulties with the availability/interpretation of paleoseismic/geologic records. Calibration of the occurrence rates for multi-segment ruptures (discussed in Section 2.2.1) is also a challenge. For these reasons, the choice of which types of ruptures to consider and the use of fault segmentation models in fault-based PSHAs are not standardized (see Stirling et al. 2012, Demircioğlu et al. 2018, Field et al. 2009).

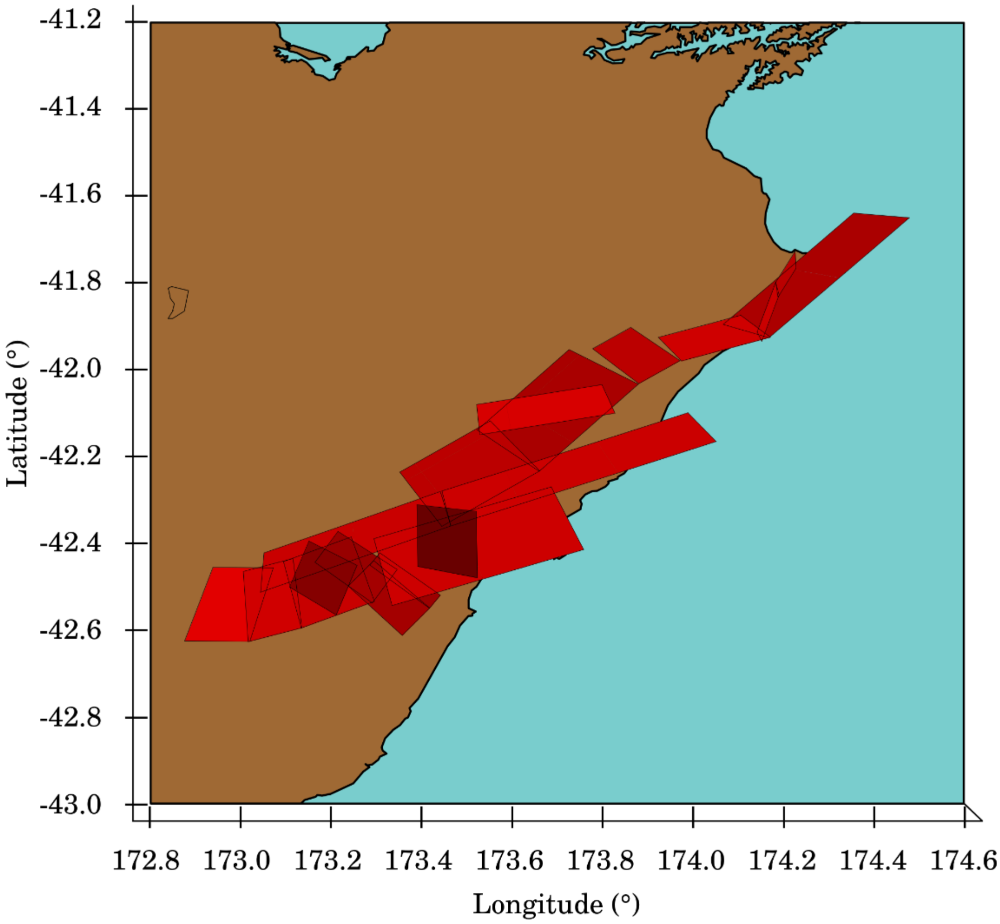

Figure 1. Approximate geometry of the multi-segment rupture that defined the 2016 M_W 7.8 Kaikōura earthquake (New Zealand).

Methods to model/generate a complete set of multi-fault ruptures have been proposed by Milner et al. (2013) and Mignan et al. (2015). Both methods are based on historical data of past events (Wesnousky 2006) and numerical analysis (Harris and Day 1993). The algorithms proposed by Milner et al. (2013) and Mignan et al. (2015) both apply fault segment geometry constraints, maximum jump distance limit, and faulting mechanism compatibility (Milner et al. 2013, Mignan et al. 2015) to assess whether two (or more) individual fault segments might create a multi-segment rupture. Mignan et al. (2015)'s algorithm does not consider floating ruptures explicitly but can account for them if the characteristic earthquake model is not used (Mignan et al. 2015). The Milner et al. (2013) methodology divides each fault segment into a large number of subsections. It generates ruptures (both floating and multi-segment) as unique sets of these subsections that pass "plausibility filters" (which comprise of geometric constraints, maximum jump distance, and Coulomb stress compatibility criteria). Since the method described by Mignan et al. (2015) was developed in a strike-slip-dominated environment, the Milner et al. (2013) method is deemed to be more general. However, the Milner et al. (2013) method is more complicated than that of Mignan et al. (2015) as it relies on static stress changes as a proxy for the dynamic stress changes (that contributes to the propagation of ruptures between faults) and uses a larger number of criteria to define the ruptures (discussed in Section 3.1). The Milner et al. (2013) method can also be considered slightly more subjective than the Mignan et al. (2015) method because it facilitates a larger number of exceptions (e.g., ruptures involving portions of left-lateral and right-lateral faults) to the rupture criteria mentioned above, which make it more adaptable to any tectonic environment.

The importance of a refined understanding of fault segmentation is yet to be fully explored in the literature. A case study developed by Valentini et al. (2020) investigated the sensitivity of seismic hazard results to segmentation variability, using a simplified version of the method used for the Uniform California Earthquake Rupture Forecast, Version 3 or UCERF3 (Field et al. 2014). The authors generated different possible multi-segment ruptures on the Wasatch fault (Utah, USA). They used a logic tree approach to account for (epistemic) uncertainties in the segmentation constraints, the slip rate model, the slip model, and the magnitude-area scaling relations (Kulkarni et al. 1984). Their analysis revealed that the segmentation procedure uncertainties are comparable or higher than epistemic uncertainties that are commonly accounted for in PSHA (e.g., slip rate model, slip model, magnitude-area scaling relations). As a result, failure to account for different segmentation procedures (or relaxing the segmentation) while developing the logic tree branches and the corresponding sensitivity analyses (Bommer and Scherbaum 2008) can significantly underestimate a seismic hazard assessment's epistemic uncertainty.

2.2 Rupture occurrence model

The rupture occurrence model most commonly used in PSHA applications is based on the Poisson process and assumes that the occurrence of events in a specific observation time window (ΔT) is not dependent on the time elapsed since the last event, T_e (i.e., there is no memory of past earthquakes). The popularity of the homogeneous Poisson model is due to (Cornell and Winterstein, 1988): (1) the fact that the sum of non-Poissonian processes may be approximated by a Poissonian one (i.e., the ability to give relatively good predictions when large areas are used as seismic sources); (2) the model only requires one parameter, termed the mean recurrence rate. This parameter is related to the coefficient a (i.e., the rate of earthquakes with magnitudes greater than the minimum magnitude of the source) in the familiar Gutenberg-Richter (Gutenberg and Richter 1944) model, which is the most commonly used MFD for PSHA studies (McGuire 2004); (3) the fact that the Poissonian assumptions result in simple and computationally efficient mathematical equations to solve for seismic hazard analysis; (4) the lack of an alternative, physically-motivated model.

Although suitable for modeling the recurrence of earthquakes on several (independent) sources (Zhuang et al. 2011), the homogeneous Poisson process is not considered appropriate for fault-based hazard assessments (Akinci et al. 2010). This may be explained by the elastic rebound theory (Reid 1910), which states that faults cyclically accumulate elastic strain energy and release it when the fault rocks' internal strength is reached. After an earthquake, the accumulated/stored energy is assumed to be at or near zero. This process is often referred to as a “renewal” process, which implies some sort of time-dependency between events, therefore violating the Poissonian assumption. Academic debates over the validity of the elastic-rebound hypothesis (and time-dependent occurrence models) have been ongoing since they were first proposed (Field et al. 2015, Mulargia et al. 2017). Lack of confidence in the elastic rebound theory can mainly be attributed to a lack of historical catalogs on large earthquakes that have ruptured the same fault segment (Stein et al. 2013). However, recent studies on time-dependent occurrence models have revealed that excluding elastic rebound leads to unrealistic aftershock statistics (e.g., Field et al. 2017). Although this result might be due to the specific aftershock simulation model examined, it represents some validation of the elastic-rebound theory (Field et al. 2017).

Time-dependent occurrence models have been used to model the recurrence of medium-to-large magnitude earthquakes on fault segments in a large number of studies, both at regional (e.g., Stirling et al. 2012, Demircioğlu et al. 2018) and more local scales (e.g., Akinci et al. 2010). They are becoming more popular than time-independent models in risk assessments for setting earthquake-insurance rates (Field et al. 2015, Mitchell-Wallace 2017). Since insurance policies are typically renewed annually (as opposed to building codes, which are generally updated every decade or so), insurance stakeholders usually apply time-dependent hazard models, where available.

Several types of time-dependent occurrence models have been proposed for PSHA. The Weibull-distributed model (Hagiwara 1974), the lognormal-distributed model (Nishenko and Buland 1987), and Brownian Passage Time (BPT) model (Ellsworth et al. 1999, Matthews et al. 2002) are amongst the most popular ones. The probability distribution functions (PDFs) of these models have two parameters, which capture the mean recurrence time (μ) and its coefficient of variation (CoV), sometimes referred to as “aperiodicity” (Convertito and Faenza 2014). Figure 2 (left panel) compares the Weibull, the lognormal, and the BPT PDFs with the same $\mu = 250yr$ and $CoV = 0.5$, as well as the exponential (Poisson, time-independent) distribution for a mean recurrence interval of 250 years.

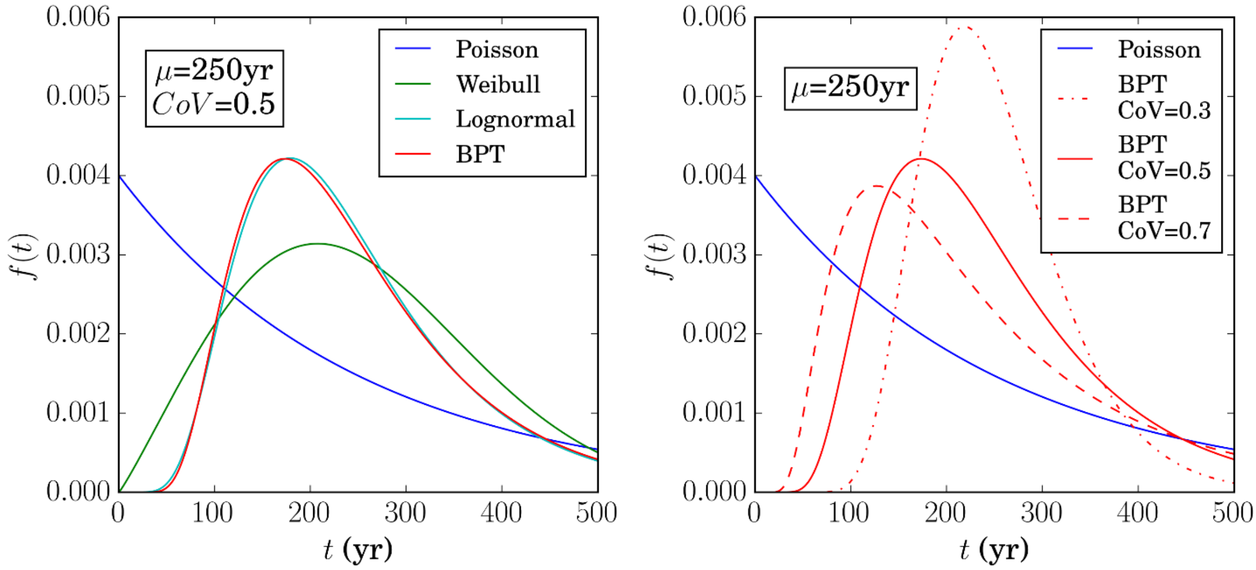

Figure 2. PDF of the interarrival time between events for some earthquake occurrence models. Left panel: comparison between the Weibull, the lognormal, and the BPT PDFs with a mean recurrence interval (μ) of 250 years and a CoV of 0.5. Right panel: comparison between three BPT distributions with a mean recurrence interval (μ) of 250 years and CoV of 0.3, 0.5, and 0.7. The exponential PDF (Poisson model) for a mean recurrence interval of 250 years is included for comparison.

Unlike the time-independent model, the expected time before the next event in a renewal process depends on the time elapsed since the last event, and the probability of occurrence of an event becomes a “conditional probability of occurrence” (conditional on the time elapsed since the last event). Consequently, all time-dependent occurrence models produce a zero (conditional) probability of event occurrence for a short time after an earthquake occurs on a given fault segment. In contrast, the Poisson process produces a constant non-zero earthquake occurrence probability (Convertito and Faenza 2014).

There is no empirical evidence that supports the use of one type of time-dependent occurrence model over another. However, amongst the several time-dependent occurrence models proposed in the literature, the BPT model has gained consensus as the preferred model for mainshock long-term time-dependency (Field et al. 2009, Field et al. 2015). This model builds upon the so-called Brownian relaxation oscillator (BRO, i.e., a superposition of a constant tectonic loading and a Brownian perturbation), and it is often preferred over Weibull or lognormal distributions for the following reasons:

- Unlike the Weibull and the lognormal, it is a physically-motivated model. In particular, the BPT model is a conceptual depiction of failure cycles in which the stress state steadily increases until reaching a chosen threshold;
- For high values of the time elapsed since the last event, the BPT probability of occurrence tends to a constant (i.e., it turns into a time-independent occurrence model), which solely depends on the fault characteristics. On the other hand, the Weibull distribution tends to infinity (i.e., ever-increasing probability of occurrence). In contrast, the lognormal distribution tends to zero, which disqualifies these distributions as reliable models according to some researchers (Convertito and Faenza 2014). This is especially the case if the mechanism of earthquake occurrence is contextualized within the process of steadily increasing load on fault.

Epistemic uncertainty in the time-dependent rupture occurrence behavior, which is due to a lack of knowledge on the underlying (unproven) elastic rebound theory, should always be accounted for in seismic hazard calculations (Field et al. 2015). This uncertainty captures one or more of the following issues: (1) the choice of a time-dependent versus a time-independent occurrence model; (2) the choice of a probability model for rupture occurrences (if a time-dependent occurrence model is chosen); and (3) the choice of the parameter values for the time-dependent occurrence model (particularly that of the CoV, which is often poorly constrained; Verdecchia et al. 2019). Figure 2 (right panel) shows example BPT distributions with different values of CoV. Uncertainties in time-dependent occurrence model parameter values are mainly due to difficulties with interpreting the geologic and paleoseismic data available for each fault, which increase the confidence interval of the calibrated CoV (e.g., Biasi et al. 2015). For instance, UCERF3 includes a logic tree with three different BPT models (with different CoVs) and a Poisson model to compute the conditional probability of rupture occurrence. Other approaches combine different time-dependent occurrence models and evaluate the conditional probability of rupture occurrence with Bayesian methods (e.g., Stirling et al. 2012, Fitzenz and Nyst 2015, Rhoades et al. 2011, Fitzenz 2018).

2.2.1 Implementation of time-independent models

The implementation of time-independent rupture occurrence models in a strictly segmented fault-based ERF involves the calibration of the occurrence rate of earthquakes on each fault (i.e., the coefficient a of the Gutenberg-Richter MFD). This rate is either inferred from geologic fault data and/or historical past event dates. The "segment total seismic moment rate conservation" criterion (e.g., Field et al. 1999, Stirling et al. 2012, Pace et al. 2016) is usually used to calibrate the rate of occurrence if geological and geomorphology data (e.g., long-term average slip rate, fault segment geometry, seismic moment budget) are available. The seismic moment rate conservation should account for the chosen MFD (e.g., Demircioğlu et al. 2018, Pace et al. 2016).

Without the segmentation hypothesis, the calibration of time-independent occurrence rates requires more advanced approaches. The 2008 Uniform California Earthquake Rupture Forecast Version 2 or UCERF2 (Petersen et al. 2007, Field et al. 2009) and previous related studies generated the ruptures coupling large segments (Section 2.1) and proceeded on a fault-by-fault basis (with expert judgment) to calibrate the time-independent occurrence rates of multi-segment ruptures. UCERF3 (Field et al. 2014, Field and Page 2011, Page et al. 2014) proposed a more objective and system-wide approach to relax the strict segmentation hypothesis and calibrate these rates. This approach utilizes the Milner et al. (2013) method to generate both floating and multi-segment ruptures (described in Section 2.1). It leverages an inversion methodology (Andrews and Schwerer 2000, Field and Page 2011, Page et al. 2014) for calibration, which involves solving an optimization problem. Each input dataset or modeling assumption (e.g., the fault segment MFD) is represented as a set of constraint equations (more details in Section 3.2). The inversion methodology can incorporate both slip rates of each single fault segment and information from paleoseismic studies. It can include every modeling assumption that can be translated into a constraint equation-set.

Three other methods to calibrate the time-independent occurrence rate of many overlapping ruptures have been proposed in the literature (SUbsectioNs of Fault in Seismic Hazard, SUNFiSH, and floating-rupture for seismic hazard, FRESH, Visini et al. 2020; Seismic Hazard and Earthquake Rate In Fault Systems, SHERIFS, Chartier et al. 2017). These three methods compute rupture rates based on the magnitude-frequency distribution (MFD) of the fault system and the available slip (or moment) rate budget to be distributed amongst the ruptures. They adopt different approaches for modeling slip rates on the fault segments, building the MFD of the earthquake ruptures, and quantifying epistemic uncertainties on the input variables. SHERIFS computes the long-term time-independent rupture occurrence rates on fault segments following an iterative process, with two constraints: the MFD of the entire fault system must follow an imposed shape, and the rate of earthquakes is calculated from the specific slip rate of each fault segment depending on all possible ruptures. Unlike UCERF3, the SHERIFS methodology does not impose an MFD shape for each fault segment and cannot account for paleoseismic data in the rupture-occurrence calibration process. Both UCERF3 and SHERIFS treat all possible combinations of multi-segment ruptures as an aleatoric uncertainty and explore the epistemic uncertainty (e.g., associated with the slip rate model, the magnitude-area scaling relation, and the slip model) using a logic tree approach (Field et al. 2014, Chartier et al. 2017).

2.2.2 Implementation of time-dependent models

Although much of the literature around time-dependent occurrence models focuses on choosing the most suitable distribution to use (BPT, lognormal, or Weibull, e.g., Abaimov et al. 2008), fewer studies have focused on their implementation within the PSHA framework. The characteristic earthquake MFD for mainshocks is often used as part of time-dependent occurrence modeling. This MFD assumes strict fault segmentation and is based on the idea that fault segments tend to periodically generate earthquakes of a characteristic size that is a function of fault length and slip rate. Its use has been justified with elastic rebound theory. The characteristic earthquake model was first proposed by Wesnousky et al. (1983) and Schwartz and Coppersmith (1984), and it has increased in popularity over the years. In fact, it has been used in many fault-based PSHA studies (e.g., Stirling et al. 2012). However, the model's rationality has been questioned in debates over the validity of the elastic-rebound hypothesis (Field et al. 2015, Mulargia et al. 2017, Kagan et al. 2012, and Geller et al. 2015). In recent years, characteristic earthquake MFDs have more commonly been used in conjunction with Gutenberg-Richter MFDs (Field et al. 2009, Field et al. 2014, Demircioğlu et al. 2018).

For strictly segmented fault models, it is straightforward to use a renewal model to compute elastic-rebound-based probabilities (e.g., Lindh 1983). The two parameters characterizing the time-dependent occurrence models (namely, μ and CoV) can be estimated in several ways depending on the available data. If a significant number of historical past event dates is available (e.g., Parkfield fault, Gonzalez et al. 2006), the adjusted maximum likelihood estimation (MLE) method can be used for model calibration (e.g., Pace et al. 2016, Ellsworth et al. 1999). Otherwise, the use of the "segment total seismic moment rate conservation" (Section 2.2.1) is now considered standard practice for calibrating the mean recurrence interval of the time-dependent occurrence model (e.g., Field et al. 1999, Stirling et al. 2012, Pace et al. 2016). In this case, a set of commonly used values (e.g., 0.3, 0.5, and 0.7; Field et al. 2009) is assumed for the CoV. More advanced calibration methods are needed when only paleoseismic studies are available and dates of past events must be estimated using probability distributions. Several of these methods use a combination of Monte Carlo sampling and MLE (e.g. Parsons 2008, Biasi et al. 2015, Pace et al. 2016), while other methods are based on Bayesian approaches (Rhoades et al. 2011, Fitzenz and Nyst 2015, Fitzenz 2018). Under the characteristic earthquake model hypothesis (i.e., the same earthquake occurrence model is valid for each point of a fault segment, Parsons 2012) one paleoseismic site along a fault segment is assumed to represent that segment's behavior in the past. It is also common to aggregate several sites' paleoseismic data along the faults (often several tens of kilometers apart) to form a unique dataset valid for the entire fault segment (Rhoades et al. 2011, Van Dissen et al. 2013).

Time-dependent probability calibration and calculations are not straightforward when strict fault segmentation and characteristic earthquake assumptions are relaxed (Field et al. 2009). This is because classic time-dependent occurrence models cannot be applied to specific fault points, as demonstrated by advanced physics-based earthquake generation simulators based on the elastic rebound theory (Tullis et al. 2012) and the simulations presented by Field (2015). Besides, paleoseismic data at a single location cannot be used to calibrate time-dependent occurrence models for an entire fault segment and aggregating paleoseismic data of several sites along a specific fault segment can lead to biased model calibration, since the ruptures could have occurred on any length of the segment (Field 2015, Parsons 2012). Thus, paleoseismic sites are essentially a point process that often cannot reveal much information about rupture dimensions or variability if fault segmentation assumptions are relaxed. However, paleoseismic data provide mean empirical earthquake rates for the specific location at which they were collected (e.g., Biasi et al. 2015), which are crucial to seismic hazard assessments (Field et al. 2014, Parsons 2012). Relaxing the segmentation assumptions also introduces the need for complex methods to compute the conditional time-dependent probabilities of rupture occurrence. The method proposed for UCERF3 (Field et al. 2015) computes the mean recurrence interval (μ) from the long-term time-independent occurrence rates and applies a magnitude-dependent set of CoVs to calculate the conditional probability of occurrence of all possible ruptures.

The challenges discussed above in quantifying rupture occurrences highlight the need for a standardized method of incorporating time-dependent occurrence models in unsegmented fault-based PSHA. This method should adequately handle all the datasets useful to calibrate the time-dependent occurrence model and avoid inconsistent results with physics-based rupture generation simulations.

2.3 Fault interaction

The term "fault interaction" often has different meanings in the literature. There are two distinct types of interaction: "inter-fault multi-rupture" and "triggering interaction". Inter-fault multi-rupture, which causes the sudden (almost instantaneous) propagation of a rupture between faults, has already been discussed in Section 2.1. Triggering interaction is the main focus of this section. This type of interaction is a later consequence of a large magnitude earthquake on neighboring faults (Stein et al. 1997) and is thought to have promoted progressive failure for some of the most recent events: the 2004–2005 M_W 9.1–8.7 Sunda megathrust (Indian Ocean) events (Mignan et al. 2006), the 1999 M_W 7.4–7.1 Izmit and Duzce (Turkey) North Anatolian earthquakes (Parsons et al. 2000, Stein et al. 1997) and the 2019 M_W 6.4–7.1 Ridgecrest (USA) sequence (Toda and Stein 2020, Wang et al. 2020). The effects of triggering fault interaction include "transient effects" and "permanent effects" (Stein et al. 1997).

Permanent effects are long-term and are usually quantified using the static coseismic Coulomb stress change (King et al. 1994) caused by a rupture on nearby faults or surrounding areas. Increasing (or decreasing) the Coulomb stress on a fault segment permanently decreases (or increases) the time required for tectonic stressing to bring a segment to failure (Stein et al. 1997), and therefore (based on the elastic rebound theory) the conditional probability of earthquake occurrence. This permanent effect is often referred to as "time advance/delay" or "clock change" (Stein 1999, Field 2007). Permanent effects of triggering interaction are usually accounted for in the PSHA framework by changing the time-dependent conditional probabilities of event occurrence on the same fault segment. Several authors estimated the coseismic Coulomb static stress changes caused by past (known) events on the North Anatolian Fault in Turkey (Parsons 2004, Murru et al. 2016). The approach used is hard to replicate in other areas of the world due to a lack of detailed information on previous events in the area of interest (e.g., the exact year of occurrence, approximate surfaces involved in the ruptures).

Transient effects are short-term increases in the probability of additional earthquakes in the area where a rupture occurs, which decay with time and distance from the first event (Toda et al. 1998). Several methodologies to include the transient effect have been proposed and evaluated in the literature (e.g., Parsons 2005 and references therein). The most common of these (e.g., Toda et al. 1998, Mignan et al. 2016) is based on the state-dependent constitutive model proposed by Dieterich (1994), which argues that several types of widely observed earthquake phenomena (e.g., aftershocks, triggered events on nearby fault segments) are short-term perturbations of the seismicity caused by stress changes from a previous shock or set of shocks (Toda et al. 1998).

Toda et al. (1998) included the fault interaction process (both transient and permanent effects) in the calculation of conditional probabilities of event occurrences on fault segments close to the 1995 M_W 6.9 Kobe earthquake (Japan). The 2002 Working Group on California Earthquake Probabilities (WGCEP) introduced a modified renewal time-dependent occurrence model called "BPT-step" (WGCEP 2002), which accounted for a change in stress caused by rupture on a nearby fault. Because the exact proximity to failure (or "state" of the system) is unknown at the time of the stress-changing event, applications of this model require an integral over all possible states of the system (Matthews et al. 2002). The WGCEP 2002 accounted for up to one stress-changing event on each segment (Field 2007). This model was not used for subsequent versions of the California earthquake rupture forecast (UCERF2) as it did not significantly impact the mean earthquake probabilities (for the specific case of California).

None of the aforementioned applications of fault interaction can capture the temporal evolution in the conditional probabilities of additional earthquake occurrence. They only evaluate the effects of the stress change at one point in time and assume that the resulting probabilities are constant throughout the forecast window. A significant step forward in incorporating fault interaction in risk assessments was presented by Mignan et al. (2016), where stochastic event sets were generated by accounting for both permanent and transient effects of fault interaction between simulated events.

In recent years, researchers have also explored the consequences of post-seismic effects on earthquake probabilities (e.g., Verdecchia et al. 2018, Verdecchia et al. 2019, Pino et al. 2019). These effects include the redistribution of Coulomb stress due to viscoelastic relaxation of the lower crust and upper mantle, which is thought to play an important role at long timescales (Verdecchia et al. 2018). Investigations of post-seismic effects after the Central Italy sequence (e.g., Verdecchia et al. 2018, Pino et al. 2019) suggest that the viscoelastic stress transfer plays a more significant role than coseismic Coulomb stress transfer in the long-term triggering of events. However, further examination and discussion of viscoelastic methods are outside the scope of this work.

2.4 Discussion

The previous three sections offer a current literature review on fault segmentation and multi-segment ruptures, time-dependent occurrence models and their implementation, and fault interaction effects between subsequent events. Table 1 provides a schematic comparison between the most recent fault-based seismic source models, based on these features.

The work carried out by Field et al. (2014), Field and Page (2011), Field et al. (2015), Milner et al. (2013), Field (2015), Field and Jordan (2015), and Page et al. (2014) for UCERF3 (California) resulted in one of the most comprehensive frameworks for fault-based seismic source modeling. Its features include (1) the relaxation of fault segmentation; (2) the inclusion of floating and multi-segment ruptures in a standardized way; (3) the consistent interpretation of available fault data (e.g., slip rates and paleoseismic data); and (4) the inclusion of time-dependent conditional probabilities of earthquake occurrence (i.e., conditional on the time elapsed since the last event).

UCERF3 was extensively tested and represented a step forward with respect to common approaches for establishing and calibrating fault-based earthquake source models (Stirling et al. 2012, Demircioğlu et al. 2018). However, some of its methods (e.g., for computing occurrence probabilities of given ruptures in a paleoseismic trench) and scaling relations rely on California-specific data. In addition, UCERF3 does not explicitly account for triggering fault interaction between major known fault segments. The UCERF3 authors assume that the aftershock model calibrated based on the UCERF3 time-dependent occurrence model (Field et al. 2015) can capture any static or dynamic triggering effects (Field et al. 2017). A procedure to explicitly incorporate both fault interaction and mainshock earthquake triggering within the PSHA framework has been proposed by Mignan et al. (2016), which builds upon the work of Dieterich (1988), Dieterich (1994), Toda et al. (1998) and Stein et al. (1997). This methodology generates the earthquake catalogs (i.e., simulated events), accounting for fault interaction with Coulomb stress changes (Section 2.3).

Table 1. Comparison between different fault-based seismic source models. MSR: Multi-segment ruptures; FR: Floating ruptures; TD: Time-dependent; MFD: Magnitude-frequency distribution.

Reference	**Region**	**MSR?**	**Floating ruptures?**	**Inclusion of TD occurrence model?**	**TD model calibration**	**MFD**	**Fault Interaction?**
Stirling et al. 2012	New Zealand	No	No	Three fault segments (around 1% of all the fault segments)	Bayesian methods (Rhoades et al., 2011)	Characteristic	No
Demircioğlu et al. 2018	Turkey	No	With MFD	No	N/A	Gutenberg-Richter	No

Field et al. 2009	UCERF2 California	Some	With MFD	36 fault segments (around 10% of all the fault segments)	Monte Carlo sampling with MLE for the mean recurrence time. Logic tree approach for the aperiodicity	Combined characteristic and Gutenberg-Richter	No
Field et al. 2015	UCERF3 California	Yes	Explicitly	All faults	Field (2015) method for the mean recurrence time. Logic tree approach for the aperiodicity	Combined characteristic and Gutenberg-Richter	No

3 Proposed framework

The proposed framework introduced in this section aims to combine a simplified version of the UCERF3 methodology with a simulation-based procedure to generate stochastic catalogs that accounts for triggering fault interaction. It consists of the following steps (shown schematically in the flowchart in Figure 3 and discussed in detail in the next sub-sections):

- Step 1 – Rupture generation: based upon the geometrical and geological characteristics of the considered fault system, this step produces a set of physically possible ruptures, accounting for floating and multi-segment rupture earthquakes (Milner et al. 2013);
- Step 2 – Inversion: combining all the available information for the considered faults (slip rates, paleoseismic data, etc.), this step solves the long term-time independent rates of all the possible ruptures, based on an objective methodology (e.g., Field and Page 2011, Field et al. 2014, Page et al. 2014);
- Step 3 – Time-dependent probabilities: based upon the results of the previous step, this step calculates time-dependent occurrence probabilities of the ruptures (Field 2015, Field and Jordan 2015, Field et al. 2015);
- Step 4 – Stochastic event generation: in this step, the stochastic event set (i.e., synthetic catalogs of earthquake ruptures) is generated
    - Step 4a – Fault interaction: this step incorporates a fault interaction proxy (i.e., Coulomb stress changes) in Step 4, which updates the time-dependent occurrence probabilities computed in Step 3 (Mignan et al. 2016, Toda et al. 1998).
- Step 5 – Hazard calculations: in this step, a GMM is applied to each event in the stochastic event set, and the hazard curves are calculated.

The main advancement of the proposed framework over the original UCERF3 methodology is its explicit incorporation of fault interaction triggering, using a procedure similar to Mignan et al. (2016) and Toda et al. (1998). This overcomes UCERF3's inconsistencies with physics-based simulators (Field 2015). The inclusion of triggering fault interaction can promote triggered events including adjacent fault segments that increase the short-interval re-rupturing probabilities in line with physics-based simulators (Field 2015). Another improvement of the proposed framework over UCERF3 is the lower number of constraints (i.e., a lower amount of input data is needed) required for the inversion procedure (Section 2.2.1 and Section 3.2), which makes it more applicable to other areas of the world. Unlike UCERF3, the proposed framework also includes the inversion constraint developed by Valentini et al. (2020) for excluding multi-segment ruptures.

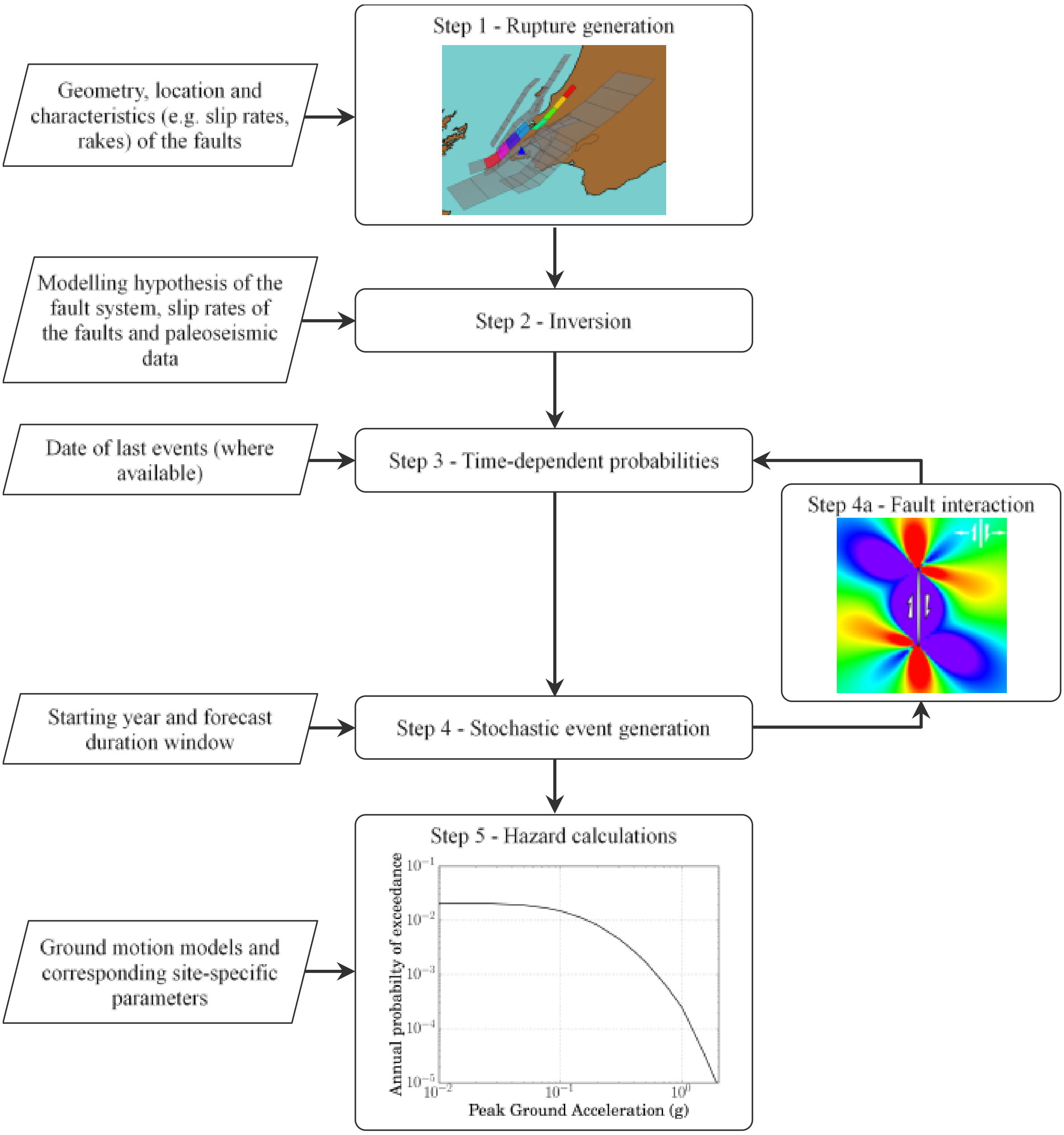

Figure 3. Schematic representation of the proposed framework.

3.1 Step 1 – Rupture generation

An ensemble of viable (i.e., physically possible) ruptures is generated, including both multi-segment and floating ruptures. The Milner et al. (2013) procedure (see Section 2.1) is used in this case. The main inputs of the rupture generation step are geometric parameters of the considered fault segments (e.g., dip angle, down-dip width, rake, latitudes and longitudes of the fault trace). Each fault segment is divided into many subsections; all subsections have approximately equal length, which is about half the seismogenic thickness. Ruptures are defined as unique sets of these subsections. They are created by iterating through all possible combinations of subsections and applying a set of filters, called "plausibility filters" to exclude non-physically sensible ruptures (Milner et al. 2013). The filters are:

- All fault segments connect within 5 km or less.
- Ruptures contain at least two subsections of any main fault segment.
- The maximum azimuth change between neighboring subsections is 60°.
- The maximum azimuth change between the first and last subsections is 60°.

- The maximum cumulative rake change is 180°.
- The maximum cumulative azimuth change, computed by summing absolute values over each neighboring subsection pair, is less than 560°.
- The potential connections between main fault segments must pass a Coulomb criterion that earthquake triggering between the two fault segments is physically reasonable. This filter is based on the concept of Coulomb linking stresses (Parsons et al. 2012), where static stress transmission is used as a proxy for dynamic rupture propagation.

The set of ruptures resulting from Milner et al. (2013) methodology represents only an approximation of the actual earthquake system (Field et al. 2014). The plausibility filters above may discard possible ruptures and include some that are less likely to occur. However, according to the findings of Field et al. (2014) and Valentini et al. (2020), this approach is a better approximation than largely ignoring multi-segment and floating ruptures, and the seismic hazard is more sensitive to the combined MFD of nearby faults, rather than the details of individual ruptures.

3.2 Step 2 – Inversion

The inversion methodology for calibrating the long-term rates of all possible ruptures was first proposed by Andrews and Schwerer (2000) and later expanded and improved by Field and Page (2011) and Page et al. (2014). The Page et al. (2014) methodology was used for UCERF3 (Field et al. 2014) and made use of a large number of relatively detailed datasets for California that included information on 31 paleoseismic sites and various slip rates estimates. The amount of inversion data used in UCERF3 are rarely available in other areas of the world. However, a simplified version of the inversion method is included in the proposed framework as most seismically-active areas of the globe generally have information on fault geometries, slip rates, and maximum magnitudes, and some paleoseismic data (New Zealand, Stirling et al. 2012; Italy, Valentini et al. 2019; Turkey, Demircioğlu et al. 2018).

The minimum input required to perform the inversion is a slip rate model providing the mean and the standard deviation of the slip rate for each subsection. Paleoseismic data (in the form of mean event rates calculated from the paleoseismic records) can also be included in the inversion process if they can be interpreted for each available investigation site (or aggregated across only nearby sites) and are associated with the closest subsection of the considered fault. The inversion method estimates the vector of long-term rates $\boldsymbol{f_r}$ of the R viable ruptures by solving an optimization problem, which comprises several systems of equations, each describing a particular constraint (i.e., equality constraint equations). The constraints of the optimization problem can be formulated as one single system of equations (Field and Page 2011):

$$\boldsymbol{A} \times \boldsymbol{f_r} = \boldsymbol{d} \tag{1}$$

in which $\boldsymbol{f_r}$ is a vector of rupture rates (f_r) to be solved for, $\boldsymbol{d}$ is a vector of data constraints, and $\boldsymbol{A}$ is the constraint matrix. These constraints can be weighted by the uncertainties (e.g., standard deviations) in the data and/or by the subjective degree of belief in the importance of a particular constraint. This framework is flexible since the constraints can be easily added or removed.

The proposed methodology uses several constraints from UCERF3 (Page et al. 2014 and Field and Page 2011):

1. There must be slip rate balancing of all the subsections that form the ruptures (computed from subsection geometries);
2. Paleoseismic event rates must match the available trench data;
3. The rate of each magnitude bin must vary smoothly along a fault segment (section smoothness constraint);
4. Subsections must have specific MFDs, which are combinations of the characteristic and the Gutenberg-Richter models (fault-segment MFD constraint).

The proposed methodology also uses so-called "improbability constraints", which can impose a lower rate for any designated event or event type and can be used to change the segmentation methodology. The first improbability constraint used in this study has been proposed by Valentini et al. (2020), which prevents the occurrence of multi-segment ruptures. The second proposed improbability constraint penalizes floating ruptures. Details on the constraints used in this study are provided in Appendix A.

Field and Page (2011) used standard linear inverse theory to solve the (relatively small) optimization problem in the least-square sense. This study uses the more efficient simulated annealing method (Kirkpatrick et al. 1983) employed by Page et al. (2014), which is a probabilistic technique for approximating the global optimum of a given function (i.e., minimize the summed squared misfit between the data and synthetics, also called energy). The simulated annealing method requires a "starting model" with a set of initial rupture rates, which can be set to null (Page et al. 2014). The specific approach adopted for the simulated annealing in the proposed framework is outlined in Page et al. (2014), which also presents extensive tests on the best settings to be used (e.g., simulated annealing perturbation functions and cooling functions). However, the solution convergence, the minimum number of iterations to achieve a sufficiently good fit, and the solution's stability must be evaluated on a case-by-case basis. It is beyond the scope of this work to investigate possible alternatives to the simulated annealing approach.

3.3 Step 3 – Time-dependent probabilities

The methodology proposed by Field (2015) and Field and Jordan (2015) and extended for UCERF3 (Field et al. 2015) is used herein to compute the conditional time-dependent probabilities of occurrence of the r^{th} rupture, P_r, which overcomes the challenges associated with time-dependent modeling for unsegmented fault assumptions (see Section 2.2). Appendix B provides the implementation details of the time-dependent probability calculations based on a BPT model and the work published by Field (2015), Field and Jordan (2015), and Field et al. (2015). One of the advantages of this methodology is the ability to apply magnitude-dependent CoV (or aperiodicity). The need for magnitude-dependent aperiodicity is proven by physics-based simulators (Field 2015, Visini and Pace 2014), and it has an intuitive explanation: evolving stress heterogeneities presumably influence more smaller events, less likely to be stress resetting events, than larger earthquakes. Table B 1 lists three sets of magnitude-dependent aperiodicity values inferred from physics-based simulations by Field (2015). Lower aperiodicity values lead to more regular (i.e., periodic) event occurrences. In contrast, higher aperiodicities have the opposite effect, causing a greater resemblance to a Poissonian process.

The inputs required to calculate the conditional probabilities are (1) the geometry of each rupture; (2) the long-term rates $\boldsymbol{f_r}$ of the ruptures (solved with the inversion process discussed in Section 3.2, or any other relevant method); (3) the date of the last event on each subsection (if available). Input (3) can be computed from historical events (i.e., the earthquake catalog) that are associated with a specific fault subsection (e.g., Field et al. 2015), or from a well-constrained paleoseismic study (e.g., Van Dissen et al. 2013). If input (3) is not available, the procedure proposed by Field and Jordan (2015) and Field et al. (2015) – for the case in which no event has occurred on the considered subsection during the open historic interval T_H (details are provided in Appendix B) – can be implemented.

3.4 Step 4 – Stochastic event generation

Figure 4 contains a flowchart of the stochastic event generation process used in the proposed methodology. The framework generates the time of the events t_i (in decimal years) on a yearly basis, starting from the annual conditional probability of occurrence P_r of the r^{th} rupture. This rate can be transformed into an equivalent time-dependent rate $\lambda_{eq,r}$ through a non-homogeneous Poisson process (Convertito and Faenza 2014):

$$\lambda_{eq,r} = -\log(1 - P_r)/w \tag{2}$$

where the observation window w is either one year (if no event is simulated within the considered year) or $1 - t_i$ (if an event is simulated within the considered year). For a time-independent occurrence model, each rupture's equivalent rate is directly equal to the corresponding long-term (Poissonian) rate from the inversion results (Section 3.2). Summing up all the equivalent rates of all the ruptures, it is possible to simulate the next event time t_i from an equivalent Poissonian distribution. This simulation procedure is similar to that proposed in Field (2015), but incorporates three additional features: (1) the annual updating of rupture occurrence probabilities; (2) the facility to generate multiple events in a year (adjusting the remaining time w as $1 - t_i$ whenever an event occurs); and (3) the inclusion of Coulomb stress interaction (Step 4a, Section 4.5).

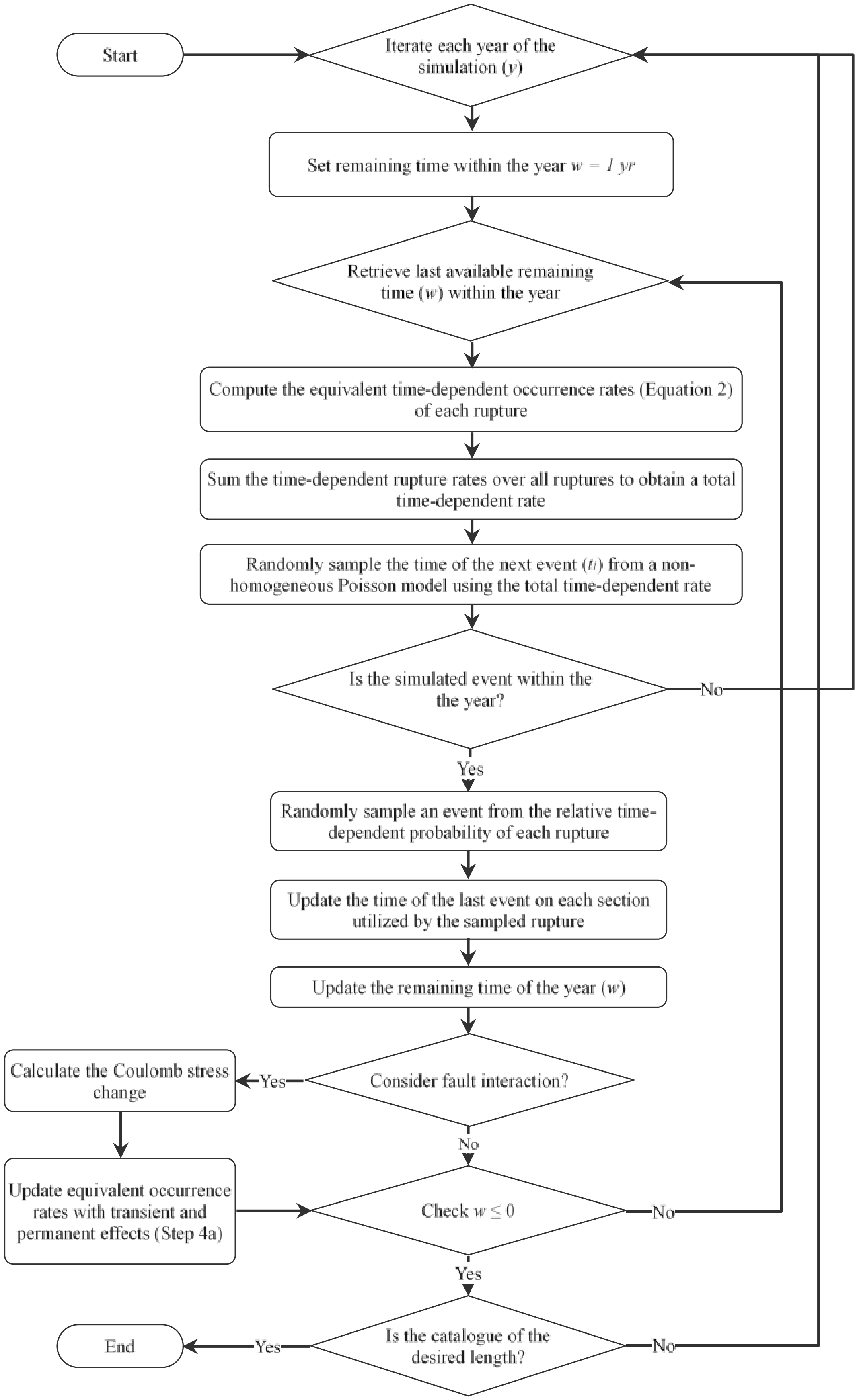

Figure 4. Flowchart of the stochastic event generation process of the complete framework (including fault interaction).

3.4.1 Step 4a – Simulate fault interaction with Coulomb stress change

Fault interaction is quantified in this study using the theory of Coulomb stress transfer (King et al. 1994; Parsons 2005), which states that the failure of a fault subsegment is promoted if the Coulomb stress increases and inhibited if the Coulomb stress decreases (Parsons 2005; Toda and Stein 2020). The stress change affects the conditional probability of rupture occurrence (Dieterich 1988; Toda et al. 1998; Murru et al. 2016) by altering the time elapsed since the last event (i.e., the permanent effect of Section 2.3) and the number of expected events in a specific time window (i.e., the transient effect of Section 2.3). Details and equations of the theory's implementation in this study are provided in Appendix C.

It could be argued that the geological slip rate and paleoseismic data may already include interaction effects from the seismic activity on nearby ruptures, which would eliminate the need to account for stress transfer. It is firstly important to note that, regardless of whether stress transfer effects are included in these data, long-term rates represent the mean (long-term) rupture behaviour and should not be affected by fluctuations due to stress transfer (e.g., Verdecchia et al. 2019). Two methods have been proposed to account for the permanent effect of a stress change (ΔCFF) in the conditional probability calculations. The first method advances the elapsed time (T_e): $T_e' = T_e + \Delta CFF/\dot{\tau}$ (i.e., clock change, Equation C 2 of Appendix C), where $\dot{\tau}$ is the tectonic stressing rate. The second approach reduces the mean recurrence time (μ): $\mu' = \mu - \Delta CFF/\dot{\tau}$ (Equation C 3 of Appendix C). Modifying the mean recurrence time changes the earthquake occurrence distribution permanently while changing the time elapsed since the last event does not affect the interarrival time distribution (Parsons 2005). The assumption that stress transfer is already included in the geological slip rate data implies that every event occurring in the vicinity of a considered fault segment can change its slip rate (and hence the long-term mean recurrence interval of possible ruptures). This is conceptually identical to modifying the mean recurrence time in Equation (C 3) of Appendix C. For this reason, changing mean recurrence times could double count the permanent effects of Coulomb stress changes. It can be argued that this problem is avoided by instead incorporating a clock change to account for fault interaction, as done in the proposed framework.

The stochastic event generation flowchart in Figure 4 incorporates the fault interaction phenomenon with a procedure similar to Mignan et al. (2016) and Toda et al. (1998). Every time an event is generated, the clock change on the neighboring (non-rupturing) subsections is evaluated using the procedure outlined in Appendix C. If known, the time elapsed since the last event is then updated and the conditional probabilities of rupture occurrence are re-evaluated. If the time since the last event is unknown, the open historic interval T_H is instead increased to emulate a positive clock change (promoting failure) or decreased to emulate a negative clock change (inhibiting failure). Illustrative examples of how the conditional probability of rupture occurrence changes when an event (i.e., a rupture) is simulated with the framework illustrated in Figure 4 are provided in Appendix D.

3.5 Step 5 – Hazard calculations

3.5.1 Ground-motion field

Ground-motion models (GMMs) provide a probabilistic distribution of ground-motion IM at a target site for a specific rupture (i.e., magnitude, site-source distance, faulting mechanism). They generally take the following functional form:

$$ln(IM) = \overline{\ln(IM)}\,(M, D, \theta) + z_E\sigma_E + z_A\sigma_A \quad (3)$$

where $ln(IM)$ represents the natural logarithm of the ground-motion IM (e.g., peak ground acceleration, PGA, or spectral acceleration, SA, at specific structural periods), which is considered to be a normally distributed random variable; $\overline{ln(IM)}$ is the logarithm of the median estimate of IM given certain predictor variables (earthquake magnitude, M, source-site distance, D and all the other parameters affecting the prediction, θ, such as the effect of style-of-faulting and soil conditions). The standard deviation of the logarithm of IM is generally partitioned into independent inter-event (σ_E) and intra-event (σ_A) standard deviations (Stafford et al. 2008). The inter-event ($z_E\sigma_E$) component of the equation captures earthquake-to-earthquake differences at the same site and the intra-event ($z_A\sigma_A$) component of the equation captures site-to-site differences for the same earthquake. The variables z_E and z_A are (independent) standard normal variables. Different GMMs are available for different tectonic settings, such as stable continental regions or subduction interfaces, as well as specific local contexts (Douglas et al. 2020). The process of selecting appropriate region-specific GMMs is beyond this study's scope, but a comprehensive review of procedures for facilitating this process can be found in Cremen et al. (2020). More details on the main variables that are typically used in GMMs (including different distance metrics and how different fault mechanisms are accounted for) can be found in Pagani et al. (2014).

For each stochastic rupture in a generated synthetic earthquake catalog, the resulting ground-motion is simulated by sampling the probability distribution defined by the GMM. The sampling process involves drawing one value of z_E and separate values of z_A at each location of interest. Spatial correlation between the ground-motions sampled at different locations and cross-correlation between the values obtained for different IM should also be considered, particularly when assessing earthquake-induced losses of building portfolios and other distributed systems (e.g., Weatherill et al. 2015, Huang and Galasso 2019). These correlations are neglected here because this study focuses on an individual target site and individual IMs.

3.5.2 Hazard curves

The n^{th} synthetic earthquake catalog contains K_n ruptures, and for each rupture, one ground-motion field is simulated as described in Section 3.5. The full set of ground-motions simulated for each rupture of synthetic earthquake catalogs can be used to derive hazard curves. Ebel and Kafka (1999) proposed a methodology for a simulation-based computation of the hazard curves, which is expressed in terms of rates of exceedance and catalog duration. An analyst can increase the accuracy and the numerical stability of the hazard curve by extending the catalog duration. However, the Ebel and Kafka (1999) method is only valid for the Poissonian (time-independent) assumption, as it does not account for the simulated events' order. A modified version of the Ebel and Kafka (1999) method is developed for this study, which produces the probability of exceeding prescribed ground-motion levels across a number of generated catalogs N with a certain duration W (e.g., N realizations of the possible earthquake catalogs of duration W years). The probability of exceeding a ground-motion level iml at a given site can be computed as:

$$P(IM > iml) = \frac{1}{N}\sum_{n=1}^{N} I(im, iml) \tag{4}$$

where im is the ground-motion at the considered site associated with a generic rupture and $I(im, iml)$ is an indicator function which returns a value of one if $im > iml$ for at least one rupture in the n^{th} catalog, zero otherwise. As the number of synthetic catalogs N increases, Equation (4) provides an increasingly more stable estimate of the probability of exceedance.

3.6 Treatment of the epistemic uncertainties

The proposed framework incorporates several sources of epistemic uncertainty: (1) fault segment geometries (e.g., dip angle); (2) the slip rate model; (3) the rupture slip model; (4) the magnitude-area scaling relation; (5) the initial setup (i.e., the hyperparameters) of the inversion algorithm (e.g., a set of initial long-term rupture rates); (6) the rupture occurrence model (e.g., time-dependent vs. time-independent, and/or the choice of time-dependent occurrence model); (7) the value of the CoV (or aperiodicity) of the time-dependent occurrence model (if used); (8) the segmentation assumptions; (9) the fault interaction process (e.g., Section 3.4.1), along with the parameters for calculating the Coulomb stress (see Appendix C); and (10) the GMM.

Uncertainty source 10 is outside the scope of this work. Field et al. (2015) included a thorough investigation of uncertainty sources 1 to 7, concluding that alternative slip rate models (source 2) produced the largest range of rupture occurrence probabilities (the highest epistemic uncertainty). The scaling relationships (source 4) were the second-largest source of epistemic uncertainty; and the considered rupture occurrence models/model parameters (sources 6 and 7) ranked third. Valentini et al. (2020) used a case study based on the Wasatch fault (Utah, USA) to investigate epistemic uncertainty sources 2 to 5, and 8. They found that the segmentation assumptions were the highest source of epistemic uncertainty, suggesting that they should be considered in a fault-based PSHA. They also concluded that the magnitude-area scaling relations and the initial setup (i.e., the hyperparameters) of the inversion algorithm have limited influence on the hazard uncertainty (differences in ground shaking for a return period are almost always within 5%). In comparison, the rupture slip models and the slip rate models in some cases show hazard differences larger than 10%. The uncertainties associated with fault interaction involve every parameter or dataset used in Coulomb stress calculations. However, some parameters like the effective coefficient of friction or the aftershock duration (see Appendix C) are often fixed to common values found in the literature (e.g., Murru et al. 2016, Stein et al. 1997, Toda et al. 1998, Parsons 2005, Mignan et al. 2016). Coulomb stress is also greatly influenced by the rupture slip model and fault segment geometries.

Preliminary sensitivity analyses have been carried out to investigate the influence of epistemic uncertainty sources 6-9 on hazard estimates obtained using the framework. A variance-based approach was adopted (e.g., Saltelli et al. 2010, Cremen and Baker 2020), which accounts for the whole probabilistic input space and measures sensitivity for an input variable in terms of its contribution to the variance of the output. The results of these sensitivity analyses reveal that the ground-motion (for several return periods and several SAs) is most sensitive to epistemic uncertainties introduced by the rupture occurrence model, followed by those of the segmentation assumptions. Future work will more thoroughly investigate all sources of epistemic uncertainty.

4 Case study

The purpose of this case study is to showcase the capabilities of the proposed framework, providing illustrative applications of time-dependent occurrence models and fault interaction in the context of unsegmented fault systems and synthetic earthquake catalog generation. The city of Wellington (New Zealand; Longitude: 174.78°, Latitude = -41.29°, shown in the left panel of Figure 5) is chosen for this case study because of the high seismicity caused by nearby faults (Stirling et al. 2012).

4.1 Available data

The Wellington-Hutt Valley segment of the Wellington fault (WellWHV), the Wairarapa (WairarapaNich) fault, and the Ohariu fault (OhariuC and OhariuS) are the principal sources of hazard for the city of Wellington (Van Dissen et al. 2013) and are considered in this study. The WellWHV fault is a right-lateral strike-slip fault. According to Rhoades et al. (2011), this fault last ruptured between 1640 and 1840 A.D; for simplicity, it is assumed to have occurred in 1740 A.D. here. A 5.80±0.74 mm/yr slip rate is used for this fault (Rhoades et al. 2011). The rupture of the entire Wellington Hutt Valley segment of the Wellington fault can produce a M_W 7.2 event (calculated with Wells and Coppersmith, 1994 relations).

The Ohariu fault segments are right-lateral strike-slip faults with different dip angles. The last event is dated between 900 and 950 A.D. (Van Dissen et al. 2013; Litchfield et al. 2010, Litchfield et al. 2004); 925 A.D. is used herein (Litchfield et al. 2010 documented the occurrence of a more recent small magnitude rupture of a limited along-strike length of the Ohariu fault in 1650 A.D., which is excluded here in line with Van Dissen et al. 2013). Rhoades et al. (2004) suggest using a uniform 1-2 mm/yr slip rate for this fault; a value of 1.5±0.5 mm/yr is therefore used herein. The rupture of both Ohariu fault segments can produce a M_W 7.3 event (calculated with Wells and Coppersmith, 1994 relations).

The WairarapaNich fault is a major active right-lateral strike-slip fault in the North Island of New Zealand. Its most recent event was a M_W 8.1 earthquake that occurred on 23 January 1855, which is presumed to have ruptured the entire (120-150 km) fault (Rodgers and Little 2006; Van Dissen et al. 2013, Carne et al. 2011; Manighetti et al. 2020). Several estimates of the slip rates along this fault segment are available, but a uniform value of 10.8±1.0 mm/yr is used for this study (Van Dissen et al. 2013; Carne et al. 2011).

Seven other nearby faults are also considered, for which rupture distances (R_{Rup}, i.e., the closest distance between the site and the rupture) are less than 20km. Table 2 shows the names and characteristics of the fault segments used in this study, and Figure 5 (left panel) shows the geometry (fault segment surface and trace) of the considered faults and their position relative to Wellington. The characteristics (Table 2) and geometries (Figure 5) of the considered fault segments are taken from Stirling et al. (2012, New Zealand Seismic Hazard Model) and other published files (https://github.com/GNS-Science/nshm-2010, last accessed 14th July 2020). Figure 5 (right panel) also reports the average long-term slip rate on the fault segment traces.

Table 2. Fault segments and characteristics used for the case study. The closest distance between Wellington city and the fault plane is less than 20km for all fault segments. Note that reported values are extracted directly from the relevant sources (column Refs) in identical format. (*) Max SD: Max seismogenic depth; (~) Char-Mw: Characteristic Mw; (/) SR: Average Long-Term Slip Rate; (^) Std SR: Standard Deviation Long-Term Slip Rate; (#) Refs: References ([1] Stirling et al. 2012 and updates, [2] Van Dissen et al. 2013, [3] Litchfield et al. 2010, [4] Litchfield et al. 2004, [5] Rodgers and Little 2006, [6] Carne et al. 2011, [7] Manighetti et al. 2020, [8] Rhoades et al. 2011).

Short Fault Name (full fault name)	**Stirling et al. 2012 ID**	**Subsection IDs**	**Length (km)**	**Max SD (*) (km)**	**Char-Mw** (~)	**Faulting Mechanism**	**SR** (/) **(mm/yr)**	**Std SR** (^) **(mm/yr)**	**Last Event Date (years AD)**	**Refs** (#)
Manaota (Mana – Otaheke)	336	0-11	91	15	7.6	Reverse	0.3	0.1	Unknown	[1]
Moonshine (Moonshine)	355	12-15	36	20	7.1	Right-lateral	0.2	0.1	Unknown	[1]
OhariuC (Ohariu Central)	362	16-19	44	20	7.2	Right-lateral	1.5	0.5	925 (900, 950)	[1], [2], [3], [4]
OhariuS (Ohariu South)	346	20-24	52	20	7.4	Right-lateral	1.5	0.5	925 (900, 950)	[1], [2], [3], [4]
Okupe (Okupe)	344	25-32	62	15	7.4	Reverse	0.8	0.2	Unknown	[1]
PukeShep (Pukerua-Shepherds Gully)	349	33-37	50	20	7.3	Right-lateral	0.5	0.15	Unknown	[1]
WairarapNich (Wairarapa-Nicholson)	345	38-46	153	35	8.2	Right-lateral	10.70	1	1855	[1], [2], [5] [6], [7]
WellWHV (Wellington Hutt Valley)	359	47-53	72	20	7.5	Right-lateral	5.8	0.74	1740 (1640, 1840)	[1], [8]
Wharekauhau (Wharekauhau Thrust)	367	54-60	50	15	7.3	Reverse	2.5	1	Unknown	[1]
Whitemans (Whitemans)	365	61-63	28	20	7.0	Reverse	0.1	0.05	Unknown	[1]

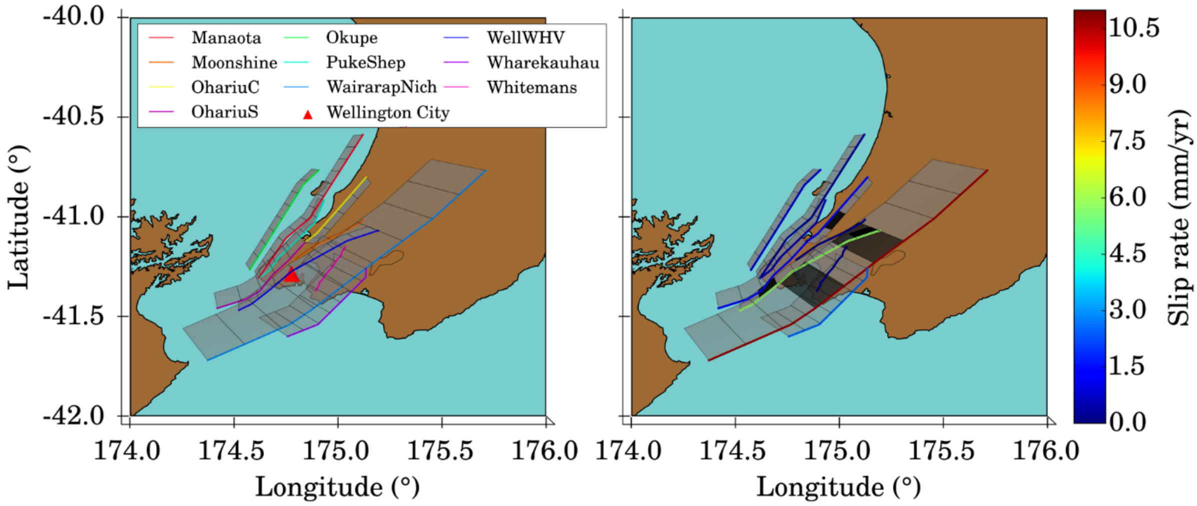

Figure 5. Left: the ten fault segments considered for the case study, divided into 64 smaller subsections. Fault traces are highlighted with a thicker line, and Wellington is marked with a red triangle. Right: slip rate and paleoseismic sites of the 64 subsections used for the inversion process. The slip rate (mm/yr) is shown on the fault trace. 3D fault subsections for which paleoseismic data are available are highlighted in a darker color.

Site-specific paleoseismic data are available for the WellWHV fault, the WairarapaNich fault, and the Ohariu fault (Rhoades et al. 2011; Van Dissen et al. 2013) at five locations. The approximate latitude and longitude of these five sites are reported in Table 3, and Figure 5 (right panel) displays the corresponding fault subsections. As explained in Section 2.2.2 and 3.2, the paleoseismic data have to be interpreted for each location (or aggregating only nearby sites) in order to be incorporated into the framework. For each site, paleoseismic event dates are uncertain and have empirically shaped probability density functions (PDFs), which are also reported in Table 3. The method proposed by Biasi et al. (2015) is used to interpret the PDFs of past event dates (Section of A.2 Appendix A) and compute the paleoseismic mean recurrence interval, along with the corresponding 2.5th, 16th, 84th, and 97.5th percentiles (Table 3).

Table 3. Paleoseismic mean rates using Biasi et al. (2015) method, including the corresponding 2.5th, 16th, 84th and 97.5th percentiles, along with the PDF of past event dates for each site.

Fault	WairarapNich	WairarapNich	OhariuC	WellWHV	WellWHV
Lat	-41.14	-41.43	-40.97	-41.34	-41.09
Lon	175.28	174.92	174.98	174.7	175.11
Mean rate	0.00082	0.0006	0.00051	0.00052	0.00105
2.5th Percentile rate	0.0006	0.00049	0.00028	0.00022	0.00055
16th Percentile rate	0.00067	0.00053	0.00036	0.0003	0.0007
84th Percentile rate	0.00099	0.00068	0.0007	0.00092	0.00156
97.5th Percentile rate	0.00112	0.00074	0.00085	0.00128	0.00198
Num events	5	5	3	4	4
Sites	Riverslea, Cross Creek and Pigeon Bush	Lake Kohangapiripiri and Turakirae Head	MacKays Crossing	Te Kopahou	Te Marua and Kaitoke
References	Van Dissen et al. 2013, Little et al. 2009	Van Dissen et al. 2013, Little et al. 2009	Van Dissen et al. 2013, Litchfield et al. 2006	Rhoades et al. 2011, Langridge et al. 2011	Rhoades et al. 2011, Langridge et al. 2011
PDF of Event 1	Uniform distribution [3260 B.C., 2890 B.C.]	Uniform distribution [4970 B.C., 4660 B.C.]	Trapezoidal distribution [3320 B.C., 3100 B.C., 2860 B.C, 2460 B.C.]	Trapezoidal distribution [2890 B.C., 2277 B.C., 650 B.C, 510 B.C.]	Uniform distribution [2280 B.C., 550 B.C.]

PDF of Event 2	Uniform distribution [1740 B.C., 1350 B.C.]	Uniform distribution [3260 B.C., 2890 B.C.]	Trapezoidal distribution [2860 B.C., 2460 B.C., 1415 B.C, 1310 B.C.]	Triangular distribution [390 B.C., 285 B.C., 115 A.D.]	Uniform distribution [255 A.D., 530 A.D.]
PDF of Event 3	Uniform distribution [350 B.C., 160 B.C]	Uniform distribution [1740 B.C., 1350 B.C.]	Uniform distribution [900 A.D., 950 A.D.]	Uniform distribution [1020 A.D., 1160 A.D.]	Uniform distribution [1055 A.D., 1220 A.D.]
PDF of Event 4	Uniform distribution [1030 A.D., 1150 A.D.]	Uniform distribution [350 B.C., 160 B.C]		Uniform distribution [1500 A.D., 1840 A.D.]	Uniform distribution [1640 A.D., 1840 A.D.]
PDF of Event 5	Historical event 1855 A.D.	Historical event 1855 A.D.			

4.2 Step 1 – Rupture generation

Following the procedure described in Section 3.1, the ten considered fault segments result in 64 subsections, (shown in Figure 5), leading to 408 plausible and feasible ruptures. Figure 6 shows an example M_W 7.5 rupture (id 213), involving the entire Ohariu Central fault (OhariuC) and approximately 40km of the Ohariu South fault (OhariuS), and a smaller M_W 6.4 rupture (id 367), involving the Wharekauhau fault.

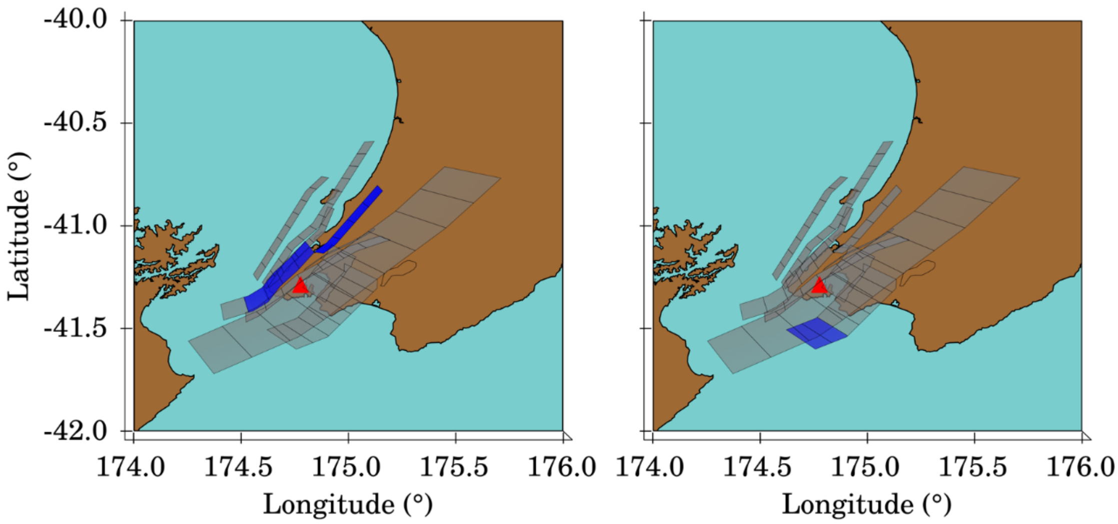

Figure 6. Left panel: example of an Mw 7.5 multi-segment rupture (id 213), involving the entire Ohariu Central fault (OhariuC) and approximately 40km of the Ohariu South fault (OhariuS). Right panel: example of an Mw 6.4 floating rupture (id 367), involving approximately 18km of the Wharekauhau fault. Wellington is marked with a red triangle.

4.3 Step 2 – Inversion

The long-term rates of the plausible ruptures are calibrated using the inversion method outlined in Section 3.2 and Appendix A. The slip rates reported in Table 2 are considered uniform along the fault segment for simplicity (consistent with Stirling et al. 2012). This implies that each subsection of the fault segments has the same slip rate as the fault segment. The paleoseismic mean rates used here are those reported in Table 3.

Three different rupture models are solved with the inversion process:

- Fully segmented rupture model (SRM), utilizing the characteristic earthquake magnitude assumption;

- No multi-segment ruptures (NMSRM), which requires that ruptures are limited to geological boundaries and cannot "jump" from one fault segment to another. However, floating ruptures are still allowed to occur;
- Unsegmented rupture model (URM), where both multi-segment ruptures and floating ruptures can occur.

The input weights of the inversion problem should be reviewed and agreed on by a panel of experts (Field et al. 2014, Page et al. 2014). The ratio between weights governs the relative importance of the associated equation-sets. The misfit of the single constraints could be used to quantitatively assess the appropriateness of the input weights (Page et al. 2014). A thorough investigation of a suitable set of input weights for the Wellington area is outside the scope of this work. A more qualitative check is performed instead (similar to Valentini et al. 2020). The following weights are used for the purpose of this study:

- Unnormalized slip rate equation-set: 100
- Normalized slip rate equation-set: 1
- Paleo event rates equation-set: 0.12
- MFD Nucleation equation-set: 0.1
- MFD Smoothness equation-set: 1000
- Multi-segment rupture segmentation equation-set: 10^9 (NMSRM and SRM)
- Floating rupture segmentation equation-set: 10^9 (only SRM)

All weights are taken from Page et al. (2014), except for those associated with paleo event rates, multi-segment rupture segmentation, and floating rupture segmentation. The paleoseismic and slip rate data are not consistent, which implies that the solver cannot lower the total energy (or the summed squared misfit) unless one of the two associated equation-sets is assigned a lower weight. Since slip rate data are considered very reliable for the faults where paleoseismic data are available (Litchfield et al. 2013), the paleoseismic event rates constraint weight is decreased by a factor of 10 with respect to the coefficient suggested by Page et al. (2014). The multi-segment rupture segmentation equation-set has been proposed by Valentini et al. (2020), and it is used here for both NMSRM and SRM. The floating rupture segmentation weight is applied in SRM. Note that assigning a weight of 10^9, compared to the other weights (of the order of 0.1 or 1), forces the solving algorithm to provide a solution (i.e., a vector of rates) that fully satisfies the corresponding equation-set (Valentini et al., 2020), i.e., results in zero total energy for that equation-set.

Once the long-term rates of all ruptures f_r are known, the long-term rates f_s of each of the 64 subsections can be computed using Equation (B 2). Figure 7 shows the comparison between the long-term (annual) rate of occurrence and the input paleoseismic rates, f_s^{paleo} in Equation (A 4). It can be observed that the inversion procedure generally produces larger occurrence rates than those of the paleoseismic data, which is reasonable given that the selected inputs weights place more importance on the slip rate equation-set. It is worth noting here that the URM and the NMSRM can better match the paleoseismic inputs because of their higher flexibility with respect to the SRM. The slip rate for the subsection can be calculated by summing up all the single-event slips (or displacements) of the ruptures (D_{sr} in Section A.1) multiplied by the corresponding long-term rates f_r, Equation (A 1). The comparison of the resulting slip rates and the input geological rates, v_s in Equation (A 1), is shown in Figure 7. It is seen that the inversion procedure produces comparable rates to those of the input data, for all three rupture models.

Figure 8 displays the implied MFD of all three rupture models. The URM MFD produces lower frequencies than that of the NMSRM, for magnitudes lower than about M_W 7.3, while the opposite is generally true for larger values. The SRM cannot produce any rupture with M_W < 7.0 (due to strict segmentation) which explains its constant frequency at the lowest magnitudes. Table 4 reports the total seismic moment release rate ($\dot{M}_{0,tot}$) implied by the New Zealand seismic hazard model (NZSHM) for a 1yr-window forecast, calculated as:

$$\dot{M}_{0,tot} = \sum_{r=1}^{R} f_r \cdot 10^{1.5M_{W,r}+9.05} \tag{5}$$

where R is the number of ruptures, f_r is defined above and $M_{W,r}$ is the corresponding moment magnitude. The published NZSHM (https://github.com/GNS-Science/nshm-2010, Stirling et al. 2012) is built with time-dependent rates for three faults. Substituting the time-dependent rates for time-independent rates (Rhoades et al. 2011, Van Dissen et al. 2013) leads to a seismic moment release rate of 2.21e18 Nm/yr. The total seismic moment release rates implied by SRM, NMSRM, and URM are between 1.87e18/yr and 1.98e18 Nm/yr (Figure 8), which is in line with the time-independent seismic moment obtained for the NZSHM. Discrepancies between the values obtained for both approaches may be due to differences between the area-magnitude conversions used or variations in the procedures adopted to calibrate the time-independent rates (Rhoades et al. 2011; Van Dissen et al. 2013).

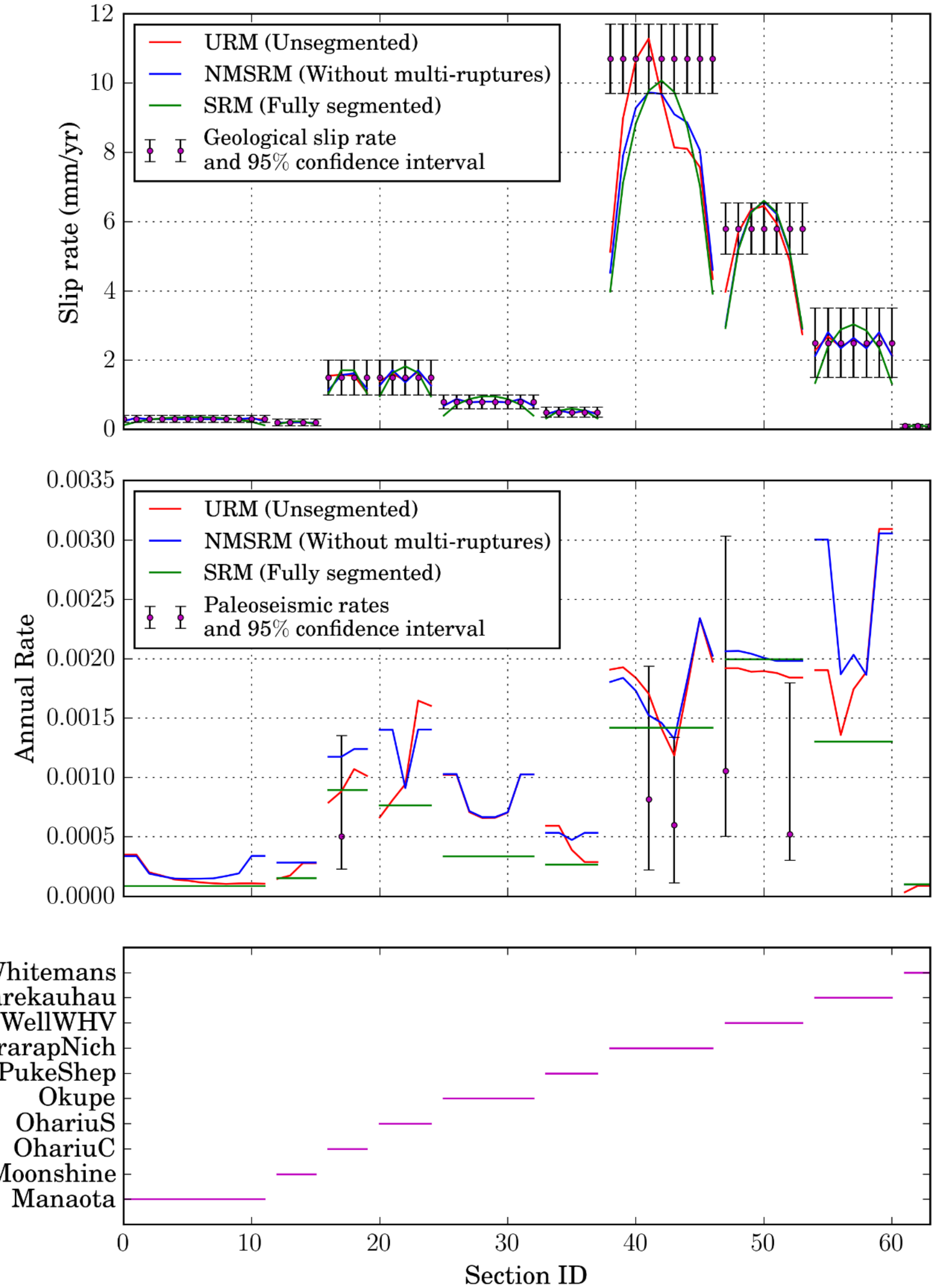

Figure 7. Top panel: slip rate of all the subsections and comparison with the input geological rates (with 95% confidence interval); mid panel: annual rate of occurrence of all the subsections and comparison with the input paleoseismic rates (with 95% confidence interval); bottom panel: graphic representation of the original fault segments and the corresponding smaller subsections ID.

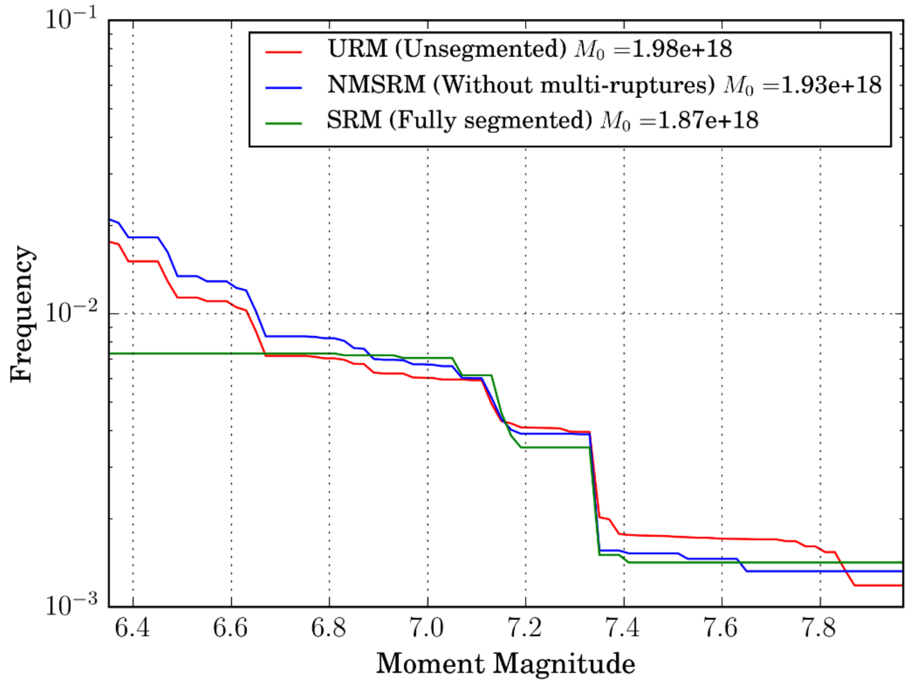

Figure 8. Magnitude-frequency distributions corresponding to the inversion solutions.

Table 4. Magnitude, annual rate, and seismic moment release rate of the considered fault segments for the original New Zealand seismic hazard model (Stirling et al. 2012). f_r (long-term annual rate), M_0 (seismic moment), $\dot{M}_0$ (seismic moment release rate).

	TI model NZSHM			
Fault name	$\boldsymbol{M_W}$	$\boldsymbol{f_r}$ **(1/yr)**	$\boldsymbol{M_0}$ **(Nm)**	$\boldsymbol{\dot{M}_0}$ **(Nm/yr)**
Manaota	7.6	4.76E-05	2.82E+20	1.34E+16
Moonshine	7.1	7.69E-05	5.01E+19	3.86E+15
OhariuC	7.2	0.00044	7.08E+19	3.11E+16
OhariuS	7.4	0.00044	1.41E+20	6.22E+16
Okupe	7.4	0.000185	1.41E+20	2.62E+16
PukeShep	7.3	0.000143	1.00E+20	1.43E+16
WairarapNich	8.2	0.0008	2.24E+21	1.79E+18
WellWHV	7.5	0.001	2.00E+20	2.00E+17
Wharekauhau	7.3	0.000714	1.00E+20	7.14E+16
Whitemans	7	5.00E-05	3.55E+19	1.77E+15
Sum ($\dot{M}_{0,tot}$)				2.21e+18

4.4 Step 3 – Time-dependent probabilities

Time-dependent probabilities are calculated according to the approach outlined in Section 3.3 and Appendix B, using the aperiodicity values associated with "medium uncertainty" in Table B 1 (i.e., 0.5 for $M_W \leq 6.7$, 0.4 for $6.7 < M_W \leq 7.2$, 0.3 for $7.2 < M_W \leq 7.7$, 0.2 for $M_W > 7.7$). The corresponding equivalent time-dependent rates $\lambda_{eq,r}$ are calculated using Equation (2). Setting 2010 as starting year (consistent with the NZSHM, Stirling et al. 2012) and a one-year time window (i.e., w = 1), Figure 9 (left panel) compares the annual (equivalent) Poissonian rates for (1) TI-URM (time-independent occurrence model with unsegmented rupture model) and (2) TD-URM (time-dependent occurrence model with unsegmented rupture model). TI-URM and TD-URM provide different results: the highest rates for TD-URM are associated with ruptures id367 and id379 (which involve small portions of the Wharekauhau thrust fault and the OhariuS fault, respectively), while the highest rates for TI-URM involve other fault segments. In particular, the highest occurrence rates for TI-URM involve the WairarapNich, WellWHV, Wharekauhau, and OhariuC/OhariuS faults. This is expected since these faults have the highest long-term average slip rates (see Table 2 and Figure 7). In TD-URM however, ruptures involving the Wellington fault (WellWHV) and the Wairarapa fault (WairarapNich) are heavily penalized with respect to TI-URM, because they are all at a relatively early stage of the earthquake cycle (last event 1740 and 1855 A.D., respectively).

Figure 9 (right panel) compares the annual (equivalent) Poissonian rates for (1) TD-URM (time-dependent occurrence model with unsegmented rupture model), (2) TD-NMSRM (time-dependent occurrence model with no multi-segment ruptures), and (3) TD-SRM (time-dependent occurrence model with a fully segmented rupture model). Unlike TD-URM and TD-NMSRM, TD-SRM rates only incorporate ruptures of entire single fault segments (consistent with the characteristic earthquake model). TD-NMSRM rates are higher than those of TD-URM on average, which is consistent with the findings of Valentini et al. (2020). This is mainly because TD-NMSRM inversion process distributes the slip rate (and the seismic moment) budget across fewer ruptures.

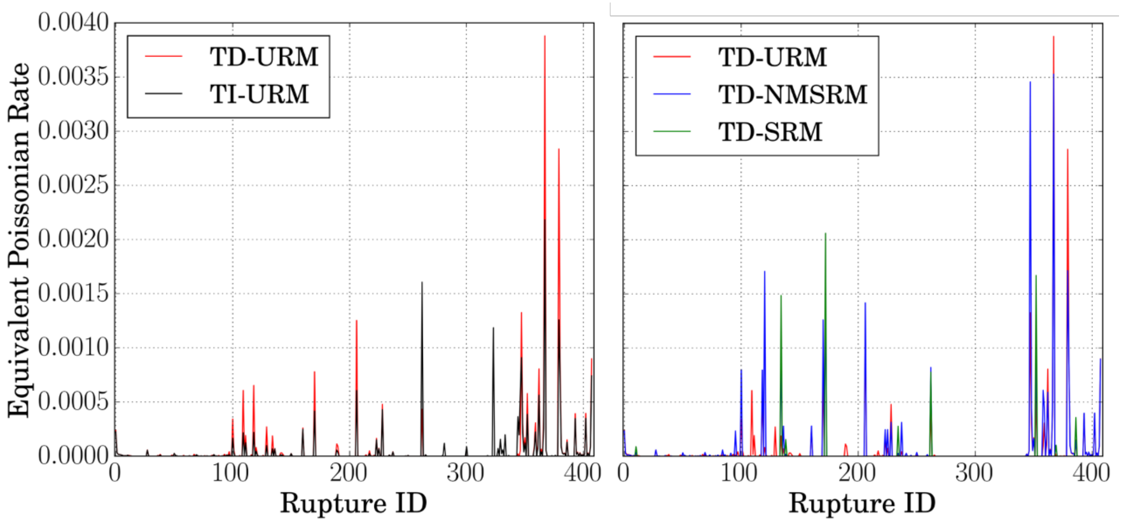

Figure 9. Left panel: comparison between TI-URM (time-independent unsegmented rupture model) and TD-URM (time-dependent unsegmented rupture model) in terms of equivalent annual Poissonian rates of the ruptures for the year 2010-2011. Right panel: comparison between TD-URM (time-dependent unsegmented rupture model), TD-NMSRM (time-dependent no multi-segment ruptures), and TD-SRM (time-dependent segmented rupture model), in terms of equivalent annual Poissonian rupture rates for the year 2010-2011.

4.5 Step 4a – Fault interaction

TD-FI-URM is the complete implementation of the proposed framework, including a time-dependent occurrence model with fault interaction (see Section 3.4.1) and an unsegmented rupture model. Figure 10 shows the clock change (in years) of the time elapsed since the last event for an example rupture (id 206). This rupture, which involves two subsections of the OhariuC fault, leads to a 200-year positive clock change of the subsection immediately adjacent to the rupture. Hence, another rupture on the OhariuC fault is promoted, meaning that there is an increased probability of any rupture that includes the red subsection in Figure 10. Conversely, the most northern subsection of the Moonshine fault experiences a negative clock change of nearly 300 years, which means that the probability of any rupture involving this subsection decreases.

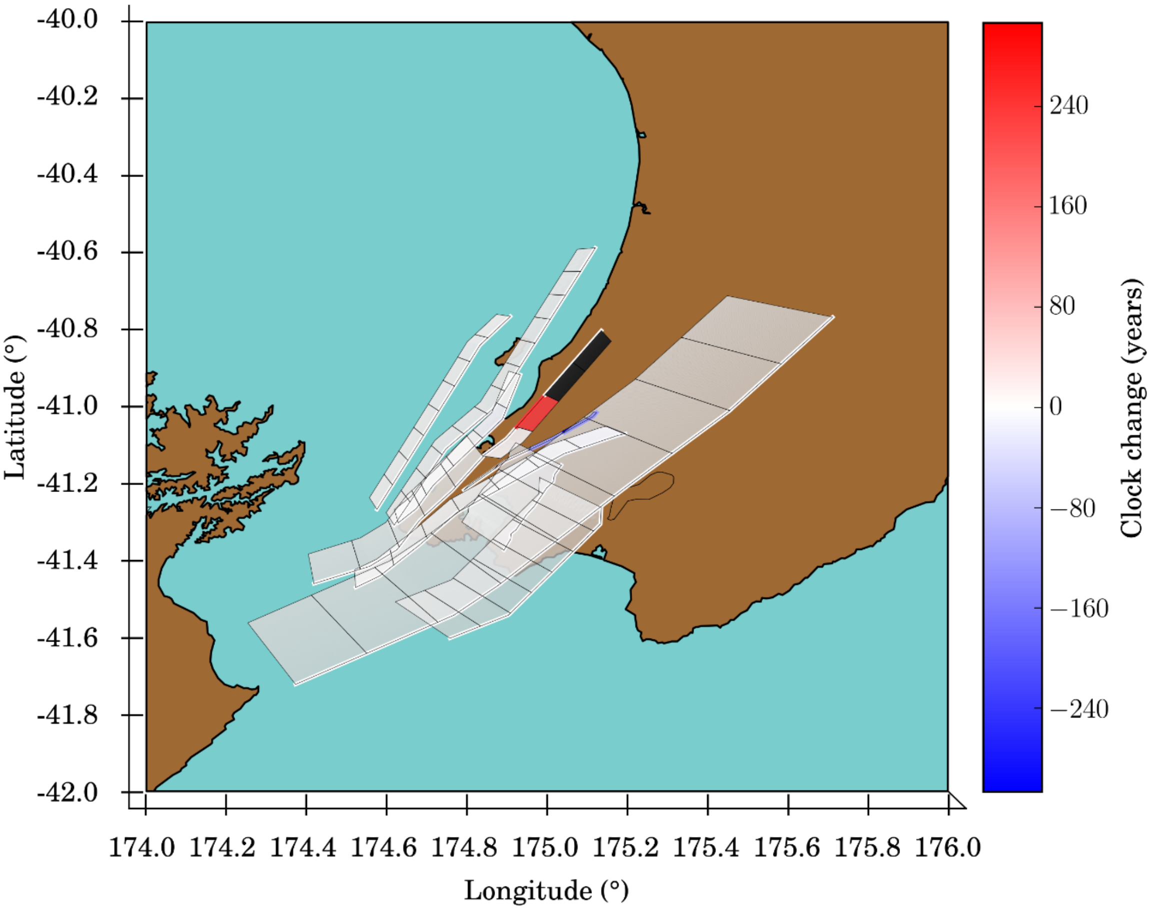

Figure 10. Clock change (in years) on fault subsections due to rupture id 206 (in black).

A total time-dependent rate is calculated for each iteration of the simulation process described in Section 3.4, representing the rate of occurrence of an earthquake generated from one of the considered faults. Figure 11 demonstrates how the total annual equivalent Poissonian rate changes over time. If no event occurs (unchanged TD-URM, grey line), the total annual equivalent rate steadily increases. The left panel displays a M_W 7.5 event (id 214, involving OhariuC and OhariuS) that occurs in the middle of 2011, and the right panel shows a M_W 6.4 event (id 367) that occurs in the middle of 2011. Following the M_W 7.5 event in the middle of 2011, TD-URM (red line) rate drops by more than 30% with respect to that of TD-URM. This is because the rate contribution of all the subsections involved in the M_W 7.5 rupture drops to zero, in line with the elastic rebound theory (Reid 1910). However, the TD-FI-URM (cyan line) rate increases in the years following the M_W 7.5 rupture due to the transient effect of the positive Coulomb stress change imposed on nearby faults (see Section C.1 Appendix C). The transient effect decreases with passing years, and this rate is eventually only influenced by the permanent effects of the Coulomb stress change (Section C.2 Appendix C). The initial increase in the TD-FI-URM rate is smaller in the right panel (M_W 6.4) for the following possible reasons:

- The nearby subsections may be too far from the rupture and/or the fault orientation may not be suitable for significant Coulomb stress changes to occur;
- The magnitude of the rupture, which is used to calculate the slip of the event (see Section C.1 of Appendix C), might be too low to produce significant Coulomb stress changes;
- The net effect of the TD-FI-URM Coulomb stress change on the nearby subsections can be low. Some subsections experience a positive Coulomb stress change, while others experience a negative one. In this case, the relative occurrence probabilities of the different ruptures will change (some ruptures are promoted while others are inhibited). However, the net effect on the total occurrence probability (or rate) of all the ruptures may remain almost unchanged. The result is a relatively small difference between the TD-FI-URM and TD-URM rates.

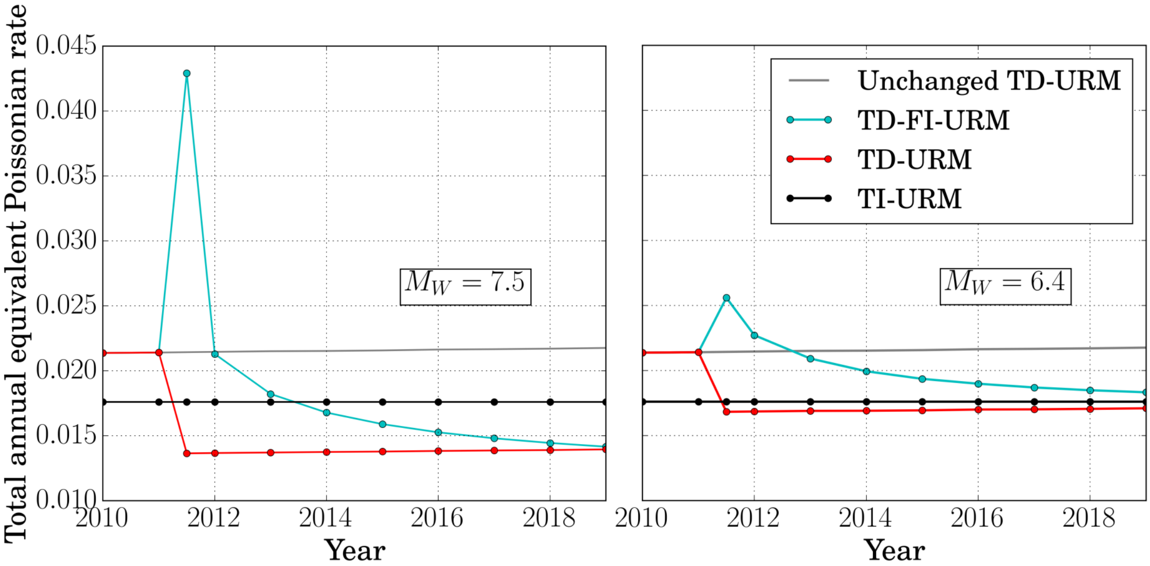

Figure 11. Change in total annual equivalent Poissonian rate due to a Mw 7.5 event (left panel) and Mw 6.4 event (right panel) for TD-FI-URM and TD-URM. TI-URM is shown for comparison.

Figure 12 shows the total rate percentage change for each of the individual ruptures occurring in the middle of 2011. The rate percentage change is calculated considering the rates of the year 2011 (before the rupture occurrence) and 2012 (after the rupture occurrence). The maximum percentage change for TD-URM (red data) is just below zero. TD-FI-URM change is generally larger than that of TD-URM (similar to Figure 11). In particular, most percentage changes for TD-FI-URM are positive, which implies that the total rate of event occurrence tends to be higher after an earthquake occurs.

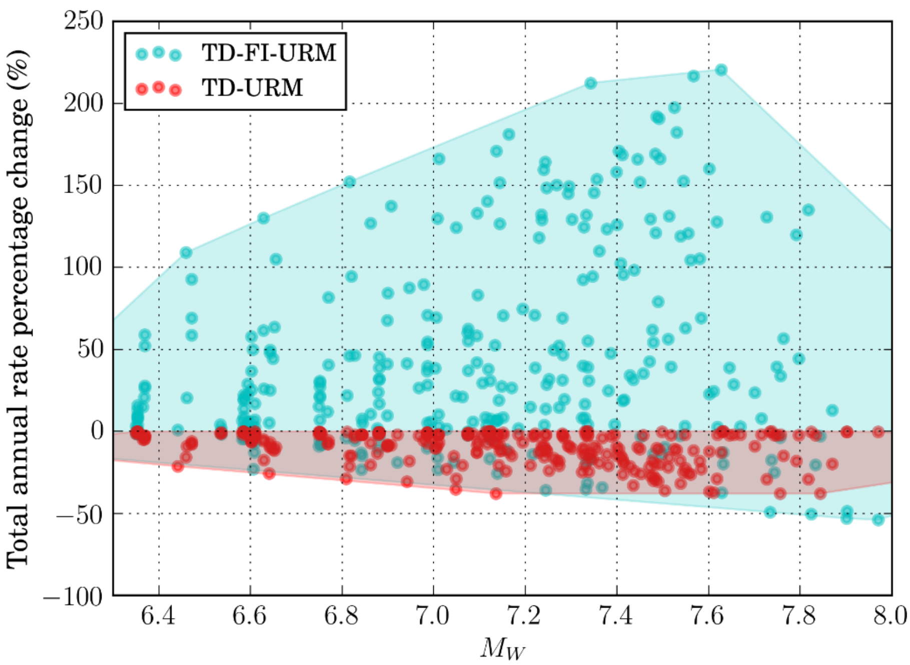

Figure 12. Change in total annual equivalent rate vs. the moment magnitude of each rupture, for both TD-FI-URM and TD-URM. The equivalent rates are calculated assuming each rupture to occur in the middle of 2011. The rate percentage change is calculated considering the rates of the year 2011 (before the rupture occurrence) and 2012 (after the rupture occurrence).

4.6 Step 5 – Stochastic event generation and hazard curves

A stochastic event set is generated for each year of a 10yr-period (2010-2019). The result is a total of 100,000 stochastic catalogs, as reported in Table 5. TI-URM does not account for the fact that the WairarapaNich fault is at a very early stage of the earthquake cycle (last rupture 1855 A.D.), which explains why the maximum magnitude for this set of models is higher than those of the other analyses. Event occurrence probabilities for TD-FI-URM are higher than those of TD-URM because of the transient increase in TD-FI-URM annual equivalent Poissonian rates (Section 4.5) after the occurrence of a rupture. The rates of TD-NMSRM are generally higher than those of TD-URM (Section 4.3), which leads to larger TD-NMSRM probabilities of event occurrence within the stochastic event set. However, the inclusion of multi-segment ruptures for TD-URM results in a higher maximum magnitude than that associated with TD-NMSRM (Section 2.1). The total annual rate of all ruptures for TD-SRM is lower than that for TD-URM, which explains the lower probabilities of occurrence for TD-SRM.

Table 5. Maximum magnitude registered in 100,000 10yr-long simulations and the occurrence probability of one, two, three, four and five events, for different analyses.

Analysis name	**Max Mw registered**	**Probability of 1 event in 10yr**	**Probability of 2 events in 10yr**	**Probability of 3 events in 10yr**	**Probability of 4 events in 10yr**	**Probability of 4 events in 10yr**
TI-URM	8.0	14.752%	1.343%	0.061%	0.001%	0.000%
TD-SRM	7.4	6.574%	0.214%	0.002%	0.000%	0.000%
TD-NMSRM	7.4	21.887%	2.819%	0.212%	0.007%	0.000%
TD-URM	7.6	17.654%	1.694%	0.076%	0.003%	0.000%
TD-FI-URM	7.6	15.810%	3.010%	0.500%	0.094%	0.013%

Ground-motion for the city of Wellington is computed using the GMM developed by Bradley (2013). The magnitude, faulting characteristics (e.g., dip, rake angles), and source-to-site distance measures are evaluated on a rupture-by-rupture case. For simplicity, a shear wave velocity in the upper 30m V_{S30} of 800m/s is used and the basin effects are accounted for as suggested by Bradley (2013). The hazard curves are computed as outlined in Section 3.5.2 and are shown in Figure 13 (for TD-URM, TD-NMSRM, TD-SRM) and Figure 14 (for TD-FI-URM, TD-URM, and TI-URM). It is worth noting that the annual probability of exceedance of low levels of ground-motion (i.e., 10^{-2} g) shown in Figure 13 and Figure 14 does not equal 1; it equates to the annual probability of occurrence of at least one rupture from the considered faults.

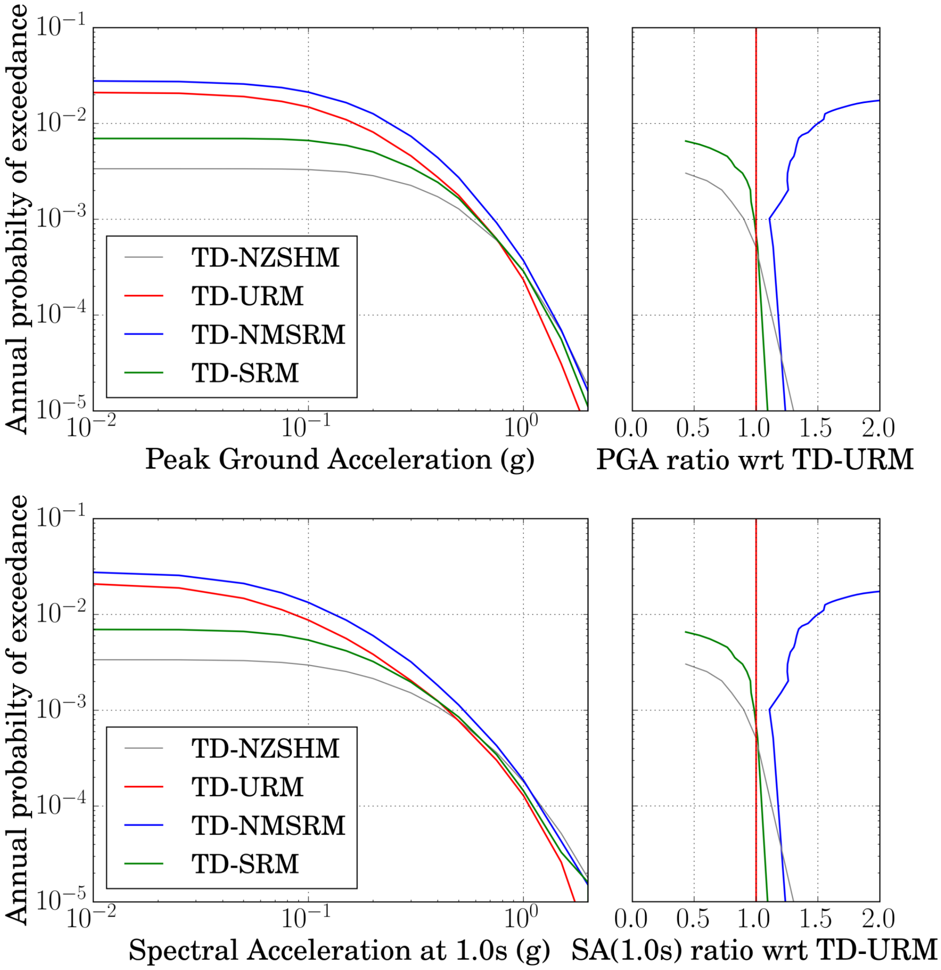

Figure 13. Comparison of the PGA and SA(1.0s) hazard curves (at the Wellington site) for TD-URM, TD-NMSRM and TD-SRM. Also shown for comparison is the corresponding hazard curve from the New Zealand seismic hazard model for a 1yr-window (TD-NZSHM). The panels on the right show the ratios of the hazard curves – with respect to TD-URM – for TD-NMSRM, TD-SRM and TD-NZSHM.

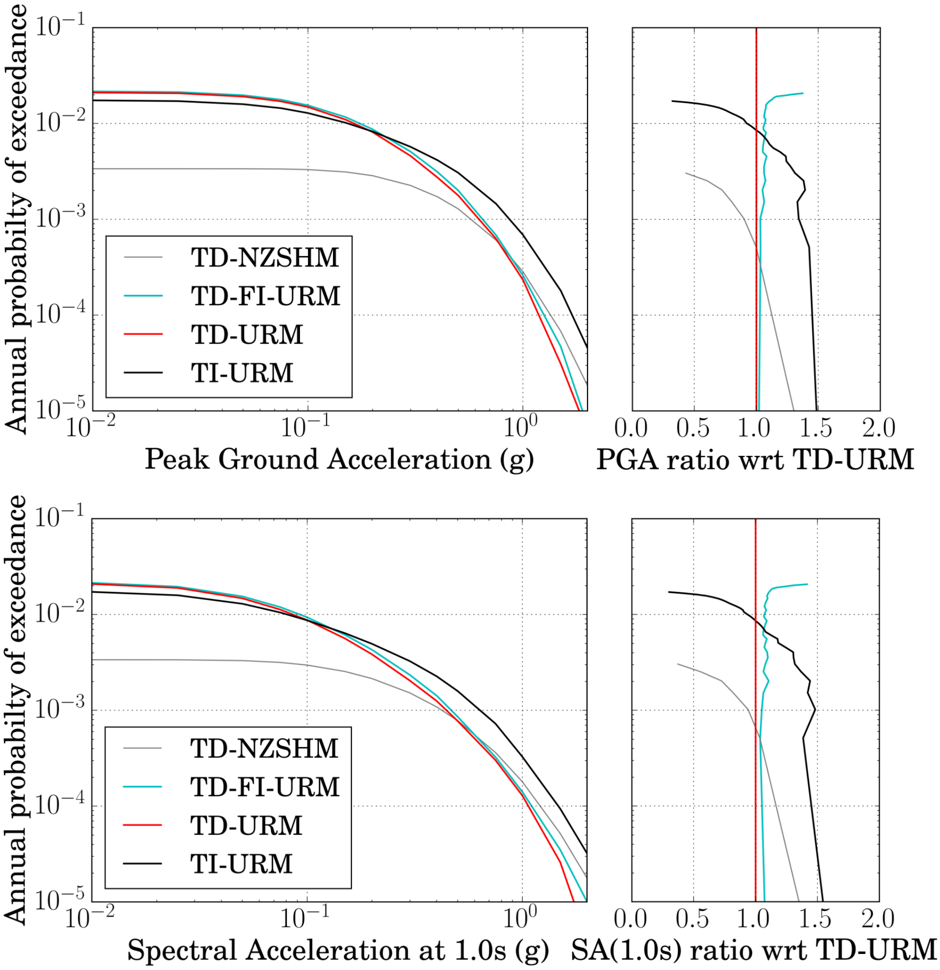

Figure 14. Comparison of the PGA and SA(1.0s) hazard curves (at the Wellington site) for TD-FI-URM, TD-URM, and TI-URM. The corresponding hazard curve from the New Zealand seismic hazard model for a 1yr-window (TD-NZSHM) is also shown for comparison. The panels on the right show the ratios of the hazard curves – with respect to TD-URM – for TD-FI-URM, TI-URM and TD-NZSHM.

5 Discussion

Section 4 outlined a simple case study to demonstrate the capabilities of the proposed framework. The methodology is flexible enough to be applied to any particular input dataset, as long as the (approximate) fault geometry and essential geologic characteristics (e.g., rake and slip rates) are available. Under the principles stated in UCERF3 (Field et al. 2014), this framework may be easily adapted to different areas of the world or extended to accommodate additional modeling assumptions. The discussion below also highlights possible extensions and shortcomings of the case study.

Figure 13 compares the hazard curves for TD-URM, TD-NMSRM, and TD-SRM for PGA and SA at 1.0s, while Figure 14 shows the same comparison for TD-FI-URM, TD-URM, and TI-URM. Both figures refer to Wellington (marked in Figure 6) and include the hazard curve (TD-NZSHM) as modeled in the NZSHM (https://github.com/GNS-Science/nshm-2010, Stirling et al. 2012) for a 1yr-window and the fault sources considered in this study (see Table 2). Note that the findings of Figure 13 and Figure 14 also hold for other SAs.

For any annual probability of exceedance, TD-NMSRM generally results in at least 15% larger ground-motion amplitudes with respect to TD-URM, which is a direct consequence of the higher TD-NMSRM event-occurrence probabilities (Table 5). For annual probabilities of exceedance higher than 10^{-3}, TD-SRM provides up to 50% lower ground-motion amplitudes with respect to TD-URM, because it does not account for any (more frequent) earthquakes with magnitudes lower than M_W 7.0 (Figure 8). TD-SRM generally provides similar results to those of TD-URM for annual probabilities less than 10^{-3}. Both TD-SRM and TD-NMSRM do not include any earthquake with a magnitude higher than M_W 7.4, which is due to the absence of multi-segment ruptures and the time-dependent occurrence model used for the WairarapaNich and the WellWHV faults (early stage of earthquake cycle). For annual probabilities of exceedance higher than around 10^{-3}, TD-SRM (i.e., considering a strict segmentation of the faults) provides a lower-bound hazard curve, and TD-NMSRM (i.e., considering only floating ruptures with no multi-segment ruptures) produces an upper-bound hazard curve (Figure 13). Considering both floating ruptures and multi-segment ruptures (which are commonly seen in nature) via an unsegmented fault model (TD-URM) like UCERF3 (Field et al. 2014) can provide an estimate of the hazard curve which always lies between the upper- and lower-bound curves for probabilities of exceedance higher than around 10^{-3} (lower than 1000-year return period). The hazard curve corresponding to TD-NZSHM is based on a strictly segmented rupture model (Stirling et al. 2012), which is why it is most similar to that of TD-SRM. Discrepancies between the curves produced by TD-SRM and TD-NZSHM arise because only three fault sources have time-dependent rates in TD-NZSHM, which are computed using Bayesian methodologies (e.g., Rhoades et al. 2011, Van Dissen et al. 2013).

The comparison of the effects of different occurrence models on the seismic hazard is shown in Figure 14. This comparison is based on the system-wide aggregated hazard of the ten considered faults and an unsegmented rupture model (URM). The shape of the seismic hazard curve for TI-URM (time-independent) is different from that for TD-URM (time-dependent). In particular, TI-URM produces ground-motion amplitudes that are over 50% lower than those of TD-URM, for probabilities of exceedance higher than around 10^{-2} (return periods lower than around 100 years). Conversely, TI-URM produces ground-motion amplitudes up to 50% higher than those of TD-URM, for lower probabilities of exceedance (return period higher than around 100 years).

Figure 14 also compares the hazard curves obtained for TD-FI-URM and TD-URM (i.e., considering and not considering the fault interaction mechanism on top of the time-dependent occurrence model). TD-FI-URM ground-motion amplitudes are within 10% of those produced by TD-URM for most annual probabilities of exceedance. While differences between TD-URM and TD-FI-URM increase for increasing annual probabilities of exceedance (i.e., low return periods), they do not become notable. However, the conclusion that the fault interaction mechanism has a negligible effect on the hazard cannot be generalized. Fault interaction is strongly dependent on the fault geometry and location, and has been found to significantly affect the hazard estimates for other areas of the world (e.g., Turkey, Stein et al. 1997; California, Toda and Stein 2020). In fact, the total rate percentage change of TD-FI-URM (Figure 12) is generally higher than that of TD-URM, and is positive for most cases (i.e., the total probability of event occurrence is higher after an earthquake). In the proposed framework, differences between TD-FI-URM and TD-URM can only arise after one rupture has been simulated. A possible improvement to the presented framework may be to adopt an approach similar to that of Stein et al. (1997) and Toda and Stein (2020), and consider the stress built-up by all known historical events until the starting year of the analysis (i.e., setting up an initial stress state). This would change the time-dependent probabilities for TD-FI-URM from the first year of the simulation, resulting in higher differences in the hazard curves.

The presented case study contains some limitations. The fault segment geometries shown in Figure 5 (from NZSHM) are idealized versions of the complex fault geometries provided by Langridge et al. (2016) and the GNS active fault database website (https://data.gns.cri.nz/af/ last accessed 14th July 2020). Since the suitability of these geometries for a site-specific study is not guaranteed, they could be revised to include additional asperities and to avoid inconsistent hazard estimates due to unrealistic fault-to-fault distances and site-to-source distances (Faure Walker et al. 2019). The simplified fault representations used may have also impacted the Coulomb stress change calculations (Section 3.4.1). Toda and Stein (2020) proposed a new approach for calculating Coulomb stresses that accounts for complex fault geometries. However, this method requires detailed focal mechanism information for a large number of past earthquakes (including small magnitude events), which reduces its general applicability.

Since only ten faults close to Wellington city are considered, possible connections with other faults are implicitly neglected in generating the 408 plausible ruptures. Moreover, according to Manighetti et al. (2020), it is possible that the M_W 7.8 2016 Kaikōura earthquake (which ruptured the Kekerengu-Needle fault) resulted in the loading of its eastern continuation, i.e., the WairarapaNich fault; this interaction is implicitly neglected in the case study. The implications of the possible connection between the Marlborough fault system, the North Island dextral fault belt, and the Hikurangi subduction zone (suggested by the 2013 Cook Strait sequence, Hamling et al. 2014) are also neglected.

The only known historical event used in the case study (i.e., known date of the last event) is that of the WairarapaNich fault (M_W 8.1 on 23 January 1855). The times of the last events for the WellWHV fault and the Ohariu faults are inferred from well-confined paleoseismic date distributions. However, this simplificaiton does not affect the results significantly. It is worth noting that the presented methodology can handle distributions of time elapsed since the last event as inputs (Field 2015). It is also assumed that the last event on the WellWHV fault, the WairarapaNich fault, and the Ohariu faults (Rhoades et al. 2011, Van Dissen et al. 2013) ruptured the entire length of the fault segments. This is probably true for the WairarapaNich fault (Van Dissen et al. 2013), but it is uncertain for the other fault segments. A refined geologic and paleoseismic study of the last event would be needed to avoid uncertainty. A further simplifying assumption is that the slip rate is uniform along the fault segment. However, the framework can account for different estimates of the slip rate in different locations, if available (Field et al. 2014).

A close analysis of the stochastic sequences (Section 4.6) for TD-FI-URM, TD-URM, and TD-NMSRM confirmed that the most frequent fault to produce a (floating) rupture is the Wharekauhau thrust fault, which is the highest contributor to seismic hazard for Wellington city. This is because the WairarapaNich and the WellWHV faults are at an early stage of the earthquake cycle and do not pose a significant hazard. The Wharekauhau thrust fault is characterized by a 2.5mm/yr slip rate (the third-highest considered, Table 2). However, the unknown date of the last event leads to a higher probability of occurrence than would be produced if the date were known or well constrained (Field and Jordan 2015). This result is not necessarily realistic because the Wharekauhau fault's slip rate is considered to be “poor quality” (Litchfield et al. 2013). Moreover, portions of the Wharekauhau fault could have ruptured with the WairarapaNich fault in 1855 (Schermer et al. 2009). Therefore, it cannot be guaranteed that the Wharekauhau fault is the most likely fault to rupture in the near future. However, it can be said that the presented methodology provides a clear means of leveraging paleoseismic campaigns and slip rate data collections to potentially better constrain the rates of earthquake occurrence.

6 Conclusions

This study has mainly focused on the fault-based ERF component of PSHA. It provided a review of the current literature on fault segmentation, multi-segment ruptures, time-dependent occurrence models, and fault interaction effects between subsequent events. Most PSHA studies neglect multi-segment ruptures and the stress interaction between faults. They also tend to use time-independent seismic hazard models, which do not capture the earthquake occurrence behavior of the elastic-rebound theory. Recent enhancements in each of these fields tend to focus on one specific aspect and neglect how one modeling assumption (e.g., segmented vs. unsegmented fault model) can affect other hypotheses (e.g., time-dependent occurrence modeling). This study collects the “best available science” in fault-based seismic hazard modeling in a unique harmonized framework, which includes (1) the fault interaction mechanism, (2) the mainshock time-dependency, and (3) an unsegmented fault model (i.e., relaxing the fault segmentation assumption).

A simple case study (consisting of Wellington city in New Zealand and ten surrounding fault segments) was used to demonstrate the proposed harmonized framework and compare:

- Time-dependent against time-independent occurrence models;
- Unsegmented fault models against models that assume strict segmentation of ruptures and “no multi-segment ruptures” (only floating ruptures); and

- Classic time-dependent occurrence models against time-dependent occurrence models that include fault interaction in the stochastic event set.

It is well known in the literature that, for a single fault segment, time-independent occurrence models can produce higher hazards with respect to time-dependent occurrence models if the time elapsed since the last event is lower than around 50% of the mean recurrence interval (Polidoro et al. 2013, Convertito and Faenza 2014; Cornell and Winterstein 1988). Comparisons between time-dependent and time-independent occurrence modeling in this study are based on several faults contributing to the hazard and on an unsegmented fault model. In this context, using a time-independent occurrence model leads to lower ground-motion amplitudes than those of the time-dependent occurrence models for low return periods (around 100 years in this study) and higher ground-motion amplitudes than those of the time-dependent occurrence models for high return periods. Furthermore, the faults with the largest contribution to the hazard differ between the time-dependent and time-independent cases. These findings can be used to inform the design of paleoseismic campaigns and slip rate data collections. Using the time-dependent component of the proposed framework generally promises more accurate hazard estimates since the considered faults' history is explicitly accounted for.

The segmentation assumption also significantly affects the hazard estimates. For higher annual probabilities of exceedance (e.g., higher than 10^{-3} in this study), considering a strict segmentation of the fault segments (consistent with the characteristic earthquake assumption) provides a lower-bound hazard curve while considering only floating ruptures (i.e., each fault segment is an independent seismic source) leads to an upper-bound hazard curve. Considering both floating ruptures and multi-segment ruptures, which are commonly seen in nature, can provide an estimate of the hazard curve which almost always lies between the upper- and lower-bound for curves (at least for the aforementioned probabilities of exceedance).

The proposed framework also includes the triggering interaction between faults (Section 2.3 and Section 3.4.1) that promotes or inhibits future events. The interaction is quantified using a simulation-based approach to generate stochastic earthquake catalogs (Mignan et al. 2016, Toda et al. 1998). For each simulated event, the fault interaction is evaluated using the Coulomb stress transfer principle, for which there is abundant evidence in both empirical and numerical studies (Toda and Stein 2020). For the considered case study, the inclusion of the fault interaction mechanism has a limited effect on the hazard that results from using classic time-dependent occurrence models: differences in ground-motion amplitudes are less than 10% for most of the annual probabilities of exceedance. However, this conclusion cannot be generalized. Fault interaction is strongly dependent on fault segment geometries, distances between fault segment surfaces, and focal mechanisms and may significantly affect the hazard estimates for other areas of the world (e.g., the North Anatolian Fault in Turkey, Stein et al. 1997, Murru et al. 2016, Stein 1999). The proposed framework could be used to check whether the fault interaction process might be significant in the considered study area.

The presented framework could be improved by accounting for the stress built-up by all known historical events that occurred until the starting year of the analysis, which may change the resulting time-dependent occurrence probabilities and seismic hazard. It could also be improved by including aftershock hazard. The vast majority of PSHA studies neglect the generation of aftershocks (and foreshocks) due to the Poissonian assumption and the declustering of earthquake catalogs (i.e., deleting aftershocks from the catalogs).

The presented harmonized framework incorporates some recent state-of-the-art enhancements in the field of seismic hazard assessment. It includes features of UCERF3 (Field et al. 2014) that enable the relaxation of fault segmentation, the inclusion of multi-segment ruptures in a standardized way, the consistent interpretation of available fault data (e.g., slip rates and paleoseismic data), and the inferring of time-dependent occurrence probabilities. It also explicitly accounts for triggering fault interaction between known faults, which is not considered in UCERF3. The framework is particularly useful for earthquake risk/loss models (Mitchell-Wallace 2017) within the (re)insurance industry, where large differences in ground-motion amplitude at low return periods could lead to significant changes in product pricing. It can produce more realistic stochastic event sets, and it is suitable for regions where active faults with known slip rates are identified.

7 Acknowledgements

We thank two anonymous reviewers for the insightful comments. Salvatore Iacoletti was supported by the UK Engineering and Physical Sciences Research Council (EPSRC), Industrial Cooperative Awards in Science & Technology (CASE) grant (Project reference: 2261161) for University College London and Willis Tower Watson (WTW), through the Willis Research Network (WRN). Gemma Cremen and Carmine Galasso are supported by the European Union's Horizon 2020 research and innovation programme under grant agreement No 821046, project TURNkey (Towards more Earthquake-resilient Urban Societies through a Multi-sensor-based Information System enabling Earthquake Forecasting, Early Warning and Rapid Response actions). Input to and feedback on the study by Dr Crescenzo Petrone and Dr Myrto Papaspiliou is greatly appreciated.

8 References

[1] Abaimov, S.G., Turcotte, D.L., Shcherbakov, R., Rundle, J.B., Yakovlev, G., Goltz, C., Newman, W.I., 2008. Earthquakes: Recurrence and Interoccurrence Times, in: Tiampo, K.F., Weatherley, D.K., Weinstein, S.A. (Eds.), Earthquakes: Simulations, Sources and Tsunamis. Birkhäuser Basel, Basel, pp. 777–795. https://doi.org/10.1007/978-3-7643-8757-0_20

[2] Akinci, A., Perkins, D., Lombardi, A.M., Basili, R., 2010. Uncertainties in probability of occurrence of strong earthquakes for fault sources in the Central Apennines, Italy. Journal of Seismology 14, 95–117. https://doi.org/10.1007/s10950-008-9142-y

[3] Andrews, D.J., 2000. Probability of Rupture of Multiple Fault Segments. Bulletin of the Seismological Society of America 90, 1498–1506. https://doi.org/10.1785/0119990163

[4] Baker, J.W., 2015. Introduction to Probabilistic Seismic Hazard Analysis. White Paper Version2.1, 77pp

[5] Bell, J.W., 1999. Surface faulting and paleoseismic history of the 1932 Cedar Mountain earthquake area, west-central Nevada, and implications for modern tectonics of the Walker Lane. Geological Society of America Bulletin 17.

[6] Bernard, P., Zollo, A., 1989. The Irpinia (Italy) 1980 earthquake: Detailed analysis of a complex normal faulting. Journal of Geophysical Research: Solid Earth 94, 1631–1647. https://doi.org/10.1029/JB094iB02p01631

[7] Biasi, G.P., Weldon, R.J., II, Dawson, T.E., 2013. Appendix F: Distribution of slip in ruptures, U.S. Geological Survey Open-File Report 2013-1165-F, and California Geol. Surv. Special Rept. 228-F

[8] Biasi, G.P., 2002. Paleoseismic Event Dating and the Conditional Probability of Large Earthquakes on the Southern San Andreas Fault, California. Bulletin of the Seismological Society of America 92, 2761–2781. https://doi.org/10.1785/0120000605

[9] Biasi, G.P., Langridge, R.M., Berryman, K.R., Clark, K.J., Cochran, U.A., 2015. Maximum-Likelihood Recurrence Parameters and Conditional Probability of a Ground-Rupturing Earthquake on the Southern Alpine Fault, South Island, New Zealand. Bulletin of the Seismological Society of America 105, 94–106. https://doi.org/10.1785/0120130259

[10] Bommer, J.J., Scherbaum, F., 2008. The Use and Misuse of Logic Trees in Probabilistic Seismic Hazard Analysis. Earthquake Spectra 24, 997–1009. https://doi.org/10.1193/1.2977755

[11] Boncio, P., Lavecchia, G., Pace, B., 2004. Defining a model of 3D seismogenic sources for Seismic Hazard Assessment applications: The case of central Apennines (Italy). Journal of Seismology 8, 407–425. https://doi.org/10.1023/B:JOSE.0000038449.78801.05

[12] Bradley, B.A., 2013. A New Zealand-Specific Pseudospectral Acceleration Ground-Motion Prediction Equation for Active Shallow Crustal Earthquakes Based on Foreign Models. Bulletin of the Seismological Society of America 103, 1801–1822. https://doi.org/10.1785/0120120021

[13] Carne, R., Little, T., Rieser, U., 2011. Using displaced river terraces to determine Late Quaternary slip rate for the central Wairarapa Fault at Waiohine River, New Zealand. New Zealand Journal of Geology and Geophysics 54, 217–236. https://doi.org/10.1080/00288306.2010.532224

[14] Chartier, T., Scotti, O., Lyon-Caen, H., Boiselet, A., 2017. Methodology for earthquake rupture rate estimates of fault networks: example for the western Corinth rift, Greece. Natural Hazards and Earth System Sciences 17, 1857–1869. https://doi.org/10.5194/nhess-17-1857-2017

[15] Convertito, V., Faenza, L., 2014. Earthquake Recurrence, in: Beer, M., Kougioumtzoglou, I.A., Patelli, E., Au, I.S.-K. (Eds.), Encyclopedia of Earthquake Engineering. Springer Berlin Heidelberg, Berlin, Heidelberg, pp. 1–21. https://doi.org/10.1007/978-3-642-36197-5_236-1

[16] Cornell, C.A., Winterstein, S.R., 1988. Temporal and Magnitude Dependence in Earthquake Recurrence Models, in: Lin, Y.K., Minai, R. (Eds.), Stochastic Approaches in Earthquake Engineering, Lecture Notes in Engineering. Springer Berlin Heidelberg, Berlin, Heidelberg, pp. 18–39. https://doi.org/10.1007/978-3-642-83252-9_2

[17] Cremen, G., Werner, M.J., Baptie, B., 2020. A New Procedure for Evaluating Ground-Motion Models, with Application to Hydraulic-Fracture-Induced Seismicity in the United Kingdom. Bulletin of the Seismological Society of America 110, 2380–2397. https://doi.org/10.1785/0120190238

[18] Demircioğlu, M.B., Şeşetyan, K., Duman, T.Y., Çan, T., Tekin, S., Ergintav, S., 2018. A probabilistic seismic hazard assessment for the Turkish territory: part II—fault source and background seismicity model. Bulletin of Earthquake Engineering 16, 3399–3438. https://doi.org/10.1007/s10518-017-0130-x

[19] DePolo, C.M., Clark, D.G., Slemmons, D.B., Ramelli, A.R., 1991. Historical surface faulting in the Basin and Range province, western North America: implications for fault segmentation. Journal of Structural Geology 13, 123–136. https://doi.org/10.1016/0191-8141(91)90061-M

[20] Dieterich, J., 1994. A constitutive law for rate of earthquake production and its application to earthquake clustering. Journal of Geophysical Research: Solid Earth 99, 2601–2618. https://doi.org/10.1029/93JB02581

[21] Dieterich, J.H., 1988. Probability of earthquake recurrence with nonuniform stress rates and time-dependent failure. Pure and Applied Geophysics 126, 589–617. https://doi.org/10.1007/BF00879011

[22] Douglas, J., 2020. Ground motion prediction equations 1964–2020, http://www.gmpe.org.uk.

[23] Ebel, J.E., Kafka, A.L., 1999. A Monte Carlo approach to seismic hazard analysis. Bulletin of the Seismological Society of America 89, 854–866.

[24] Eberhart-Phillips, D., 2003. The 2002 Denali Fault Earthquake, Alaska: A Large Magnitude, Slip-Partitioned Event. Science 300, 1113–1118. https://doi.org/10.1126/science.1082703

[25] Ellsworth, W.L., Matthews, M.V., Nadeau, R.M., Nishenko, S.P., Reasenberg, P.A., Simpson R.W., 1999, A physically-based earthquake recurrence model for estimation of long-term probabilities: U.S. Geological Survey Open-File Report 99–520, 22 p., http://geopubs.wr.usgs.gov/open-file/of99-522/

[26] Emre, Ö., Duman, T.Y., Özalp, S., Şaroğlu, F., Olgun, Ş., Elmacı, H., Çan, T., 2018. Active fault database of Turkey. Bulletin of Earthquake Engineering 16, 3229–3275. https://doi.org/10.1007/s10518-016-0041-2

[27] Faure Walker, J.P., Visini, F., Roberts, G., Galasso, C., McCaffrey, K., Mildon, Z., 2019. Variable Fault Geometry Suggests Detailed Fault-Slip-Rate Profiles and Geometries Are Needed for Fault-Based Probabilistic Seismic Hazard Assessment (PSHA). Bulletin of the Seismological Society of America 109, 110–123. https://doi.org/10.1785/0120180137

[28] Field, E.H., 2007. A Summary of Previous Working Groups on California Earthquake Probabilities. Bulletin of the Seismological Society of America 97, 1033–1053. https://doi.org/10.1785/0120060048

[29] Field, E.H., 2015. All Models Are Wrong, but Some Are Useful. Seismological Research Letters 86, 291–293. https://doi.org/10.1785/02201401213

[30] Field, E.H., 2015. Computing Elastic-Rebound-Motivated Earthquake Probabilities in Unsegmented Fault Models: A New Methodology Supported by Physics-Based Simulators. Bulletin of the Seismological Society of America 105, 544–559. https://doi.org/10.1785/0120140094

[31] Field, E.H., Arrowsmith, R.J., Biasi, G.P., Bird, P., Dawson, T.E., Felzer, K.R., Jackson, D.D., Johnson, K.M., Jordan, T.H., Madden, C., Michael, A.J., Milner, K.R., Page, M.T., Parsons, T., Powers, P.M., Shaw, B.E., Thatcher, W.R., Weldon, R.J., Zeng, Y., 2014. Uniform California Earthquake Rupture Forecast, Version 3 (UCERF3)-The Time-Independent Model. Bulletin of the Seismological Society of America 104, 1122–1180. https://doi.org/10.1785/0120130164

[32] Field, E.H., Biasi, G.P., Bird, P., Dawson, T.E., Felzer, K.R., Jackson, D.D., Johnson, K.M., Jordan, T.H., Madden, C., Michael, A.J., Milner, K.R., Page, M.T., Parsons, T., Powers, P.M., Shaw, B.E., Thatcher, W.R., Weldon, R.J., Zeng, Y., 2015. Long-Term Time-Dependent Probabilities for the Third Uniform California Earthquake Rupture Forecast (UCERF3). Bulletin of the Seismological Society of America 105, 511–543. https://doi.org/10.1785/0120140093

[33] Field, E.H., Dawson, T.E., Felzer, K.R., Frankel, A.D., Gupta, V., Jordan, T.H., Parsons, T., Petersen, M.D., Stein, R.S., Weldon, R.J., Wills, C.J., 2009. Uniform California Earthquake Rupture Forecast,

Version 2 (UCERF 2). Bulletin of the Seismological Society of America 99, 2053–2107. https://doi.org/10.1785/0120080049

[34] Field E.H., Jackson D.D., Dolan J.F., 1999. A mutually consistent seismic-hazard source model for southern California, Bulletin of the Seismological Society of America, 89, 559–578.

[35] Field, E.H., Jordan, T.H., 2015. Time-Dependent Renewal-Model Probabilities When Date of Last Earthquake is Unknown. Bulletin of the Seismological Society of America 105, 459–463. https://doi.org/10.1785/0120140096

[36] Field, E.H., Jordan, T.H., Cornell, C.A., 2003. OpenSHA: A Developing Community-modeling Environment for Seismic Hazard Analysis. Seismological Research Letters 74, 406–419. https://doi.org/10.1785/gssrl.74.4.406

[37] Field, E.H., Milner, K.R., Hardebeck, J.L., Page, M.T., van der Elst, N., Jordan, T.H., Michael, A.J., Shaw, B.E., Werner, M.J., 2017. A Spatiotemporal Clustering Model for the Third Uniform California Earthquake Rupture Forecast (UCERF3-ETAS): Toward an Operational Earthquake Forecast. Bulletin of the Seismological Society of America 107, 1049–1081. https://doi.org/10.1785/0120160173

[38] Field, E.H., Page, M.T., 2011. Estimating Earthquake-Rupture Rates on a Fault or Fault System. Bulletin of the Seismological Society of America 101, 79–92. https://doi.org/10.1785/0120100004

[39] Fitzenz, D.D., 2018. Conditional Probability of What? Example of the Nankai Interface in Japan. Bulletin of the Seismological Society of America 108, 3169–3179. https://doi.org/10.1785/0120180016

[40] Fitzenz, D.D., Nyst, M., 2015. Building Time-Dependent Earthquake Recurrence Models for Probabilistic Risk Computations. Bulletin of the Seismological Society of America 105, 120–133. https://doi.org/10.1785/0120140055

[41] Geller, R.J., Mulargia, F., Stark, P.B., 2015. Why We Need a New Paradigm of Earthquake Occurrence, in: Morra, G., Yuen, D.A., King, S.D., Lee, S.-M., Stein, S. (Eds.), Geophysical Monograph Series. John Wiley & Sons, Inc, Hoboken, NJ, pp. 183–191. https://doi.org/10.1002/9781118888865.ch10

[42] Goda, K., Petrone, C., De Risi, R., Rossetto, T., 2017. Stochastic coupled simulation of strong motion and tsunami for the 2011 Tohoku, Japan earthquake. Stochastic Environmental Research and Risk Assessment 31, 2337–2355. https://doi.org/10.1007/s00477-016-1352-1

[43] González, Á., Gómez, J.B., Pacheco, A.F., 2006. Updating seismic hazard at Parkfield. Journal of Seismology 10, 131–135. https://doi.org/10.1007/s10950-005-9005-8

[44] Gutenberg, B., Richter, C.F., 1944. Frequency of earthquakes in California. Bulletin of the Seismological Society of America 34, 185–188.

[45] Hagiwara, Y., 1974. Probability of earthquake occurrence as obtained from a Weibull distribution analysis of crustal strain. Tectonophysics, Focal processes and the prediction of earthquakes 23, 313–318. https://doi.org/10.1016/0040-1951(74)90030-4.

[46] Hamling, I.J., D'Anastasio, E., Wallace, L.M., Ellis, S., Motagh, M., Samsonov, S., Palmer, N., Hreinsdóttir, S., 2014. Crustal deformation and stress transfer during a propagating earthquake sequence: The 2013 Cook Strait sequence, central New Zealand. Journal of Geophysical Research: Solid Earth 119, 6080–6092. https://doi.org/10.1002/2014JB011084

[47] Hamling, I.J., Hreinsdóttir, S., Clark, K., Elliott, J., Liang, C., Fielding, E., Litchfield, N., Villamor, P., Wallace, L., Wright, T.J., D'Anastasio, E., Bannister, S., Burbidge, D., Denys, P., Gentle, P., Howarth, J., Mueller, C., Palmer, N., Pearson, C., Power, W., Barnes, P., Barrell, D.J.A., Van Dissen, R., Langridge, R., Little, T., Nicol, A., Pettinga, J., Rowland, J., Stirling, M., 2017. Complex multifault rupture during the 2017 Mw 7.8 Kaikōura earthquake, New Zealand. Science 356, eaam7194. https://doi.org/10.1126/science.aam7194

[48] Hanks, T.C., Bakun, W.H., 2008. M-logA Observations for Recent Large Earthquakes. Bulletin of the Seismological Society of America 98, 490–494. https://doi.org/10.1785/0120070174

[49] Harris, R.A., Day, S.M., 1993. Dynamics of fault interaction: parallel strike-slip faults. Journal of Geophysical Research: Solid Earth 98, 4461–4472. https://doi.org/10.1029/92JB02272

[50] Huang, C., Galasso, C., 2019. Ground-motion intensity measure correlations observed in Italian strong-motion records. Earthquake Engineering & Structural Dynamics 48, 1634–1660. https://doi.org/10.1002/eqe.3216

[51] Iezzi, F., Roberts, G., Walker, J.F., Papanikolaou, I., 2019. Occurrence of partial and total coseismic ruptures of segmented normal fault systems: Insights from the Central Apennines, Italy. Journal of Structural Geology 126, 83–99. https://doi.org/10.1016/j.jsg.2019.05.003

[52] Kagan, Y.Y., Jackson, D.D., Geller, R.J., 2012. Characteristic Earthquake Model, 1884-2011, R.I.P. Seismological Research Letters 83, 951–953. https://doi.org/10.1785/0220120107

[53] King, G.C.P., Stein, R.S., Lin, J., 1994. Static stress changes and the triggering of earthquakes. Bulletin of the Seismological Society of America 84, 935–953

[54] Kirkpatrick, S., Gelatt, C.D., Vecchi, M.P., 1983. Optimization by Simulated Annealing. Science 220, 671–680. https://doi.org/10.1126/science.220.4598.671

[55] Kulkarni, R.B., Youngs, R.R., and Coppersmith, K.J., 1984. Assessment of confidence intervals for results of seismic hazard analysis, in Proceedings, Eighth World Conference on Earthquake Engineering, vol. 1, San Francisco, pp. 263–270

[56] Langridge, R., Van Dissen, R., Rhoades, D., Villamor, P., Little, T., Litchfield, N., Clark, K., Clark, D., 2011. Five Thousand Years of Surface Ruptures on the Wellington Fault, New Zealand: Implications for Recurrence and Fault Segmentation. Bulletin of the Seismological Society of America 101, 2088–2107. https://doi.org/10.1785/0120100340

[57] Langridge, R.M., Ries, W.F., Litchfield, N.J., Villamor, P., Dissen, R.V., Barrell, D.J.A., Rattenbury, M.S., Heron, D.W., Haubrock, S., Townsend, D.B., Lee, J.M., Berryman, K.R., Nicol, A., Cox, S.C., Stirling, M.W., 2016. The New Zealand Active Faults Database. New Zealand Journal of Geology and Geophysics 59, 86–96. https://doi.org/10.1080/00288306.2015.1112818

[58] Lindh, A.G., 1983. Estimates of long-term probabilities of large earthquakes along selected fault segments of the San Andreas fault system in California, U.S. Geological Survey Open-File Report 83-63, 1–15

[59] Litchfield, N., van Dissen, R., Hemphill-Haley, M., Townsend, D., Heron, D., 2010. Post c. 300 year rupture of the Ohariu Fault in Ohariu Valley, New Zealand. New Zealand Journal of Geology and Geophysics 53, 43–56. https://doi.org/10.1080/00288301003631780

[60] Litchfield, N., Van Dissen, R., Heron, D., Rhoades, D., 2006. Constraints on the timing of the three most recent surface rupture events and recurrence interval for the Ohariu Fault: Trenching results from MacKays Crossing, Wellington, New Zealand. New Zealand Journal of Geology and Geophysics 49, 57–61. https://doi.org/10.1080/00288306.2006.9515147

[61] Litchfield, N., Van Dissen, R., Langridge, R., Heron, D., Prentice, C., 2004. Timing of the most recent surface rupture event on the Ohariu Fault near Paraparaumu, New Zealand. New Zealand Journal of Geology and Geophysics 47, 123–127. https://doi.org/10.1080/00288306.2004.9515041

[62] Litchfield, N.J., Van Dissen, R., Sutherland, R., Barnes, P.M., Cox, S.C., Norris, R., Beavan, R.J., Langridge, R., Villamor, P., Berryman, K., Stirling, M., Nicol, A., Nodder, S., Lamarche, G., Barrell, D.J.A., Pettinga, J.R., Little, T., Pondard, N., Mountjoy, J., Clark, K., 2013. A model of active faulting in New Zealand: fault zone parameter descriptions. GNS Science Report 2012/19. 120pp.

[63] Little, T.A., Van Dissen, R., Schermer, E., Carne, R., 2009. Late Holocene surface ruptures on the southern Wairarapa fault, New Zealand: Link between earthquakes and the uplifting of beach ridges on a rocky coast. Lithosphere 1, 4–28. https://doi.org/10.1130/L7.1

[64] Manighetti, I., Perrin, C., Gaudemer, Y., Dominguez, S., Stewart, N., Malavieille, J., Garambois, S., 2020. Repeated giant earthquakes on the Wairarapa fault, New Zealand, revealed by Lidar-based paleoseismology. Scientific Reports 10, 2124. https://doi.org/10.1038/s41598-020-59229-3

[65] Matthews, M.V., Ellsworth, W.L., Reasenberg, P.A., 2002. A Brownian Model for Recurrent Earthquakes. Bulletin of the Seismological Society of America 92, 2233–2250. https://doi.org/10.1785/0120010267

[66] McGuire, R.K., 2004. Seismic hazard and risk analysis. Earthquake Engineering Research Institute

[67] Mignan, A., Danciu, L., Giardini, D., 2015. Reassessment of the Maximum Fault Rupture Length of Strike-Slip Earthquakes and Inference on Mmax in the Anatolian Peninsula, Turkey. Seismological Research Letters 86, 890–900. https://doi.org/10.1785/0220140252

[68] Mignan, A., Danciu, L., Giardini, D., 2016. Considering large earthquake clustering in seismic risk analysis. Natural Hazards. https://doi.org/10.1007/s11069-016-2549-9

[69] Mignan, A., King, G., Bowman, D., Lacassin, R., Dmowska, R., 2006. Seismic activity in the Sumatra–Java region prior to the December 26, 2004 (Mw=9.0–9.3) and March 28, 2005 (Mw=8.7) earthquakes. Earth and Planetary Science Letters 244, 639–654. https://doi.org/10.1016/j.epsl.2006.01.058

[70] Milner, K.R., Page, M.T., Field, E.H., Parsons, T., Biasi, G.P., Shaw B.E., 2013. Appendix T: Defining the inversion rupture set via plausibility filters, U.S. Geological Survey Open-File Report 2013-1165-T, and California Geol. Surv. Special Rept. 1792T, 14 pp.

[71] Mitchell-Wallace, K. (Ed.), 2017. Natural catastrophe risk management and modelling: a practitioner's guide. John Wiley and Sons, Inc, Hoboken, NJ.

[72] Mulargia, F., Stark, P.B., Geller, R.J., 2017. Why is Probabilistic Seismic Hazard Analysis (PSHA) still used? Physics of the Earth and Planetary Interiors 264, 63–75. https://doi.org/10.1016/j.pepi.2016.12.002

[73] Murru, M., Akinci, A., Falcone, G., Pucci, S., Console, R., Parsons, T., 2016. $M \geq 7$ earthquake rupture forecast and time-dependent probability for the sea of Marmara region, Turkey. Journal of Geophysical Research: Solid Earth 121, 2679–2707. https://doi.org/10.1002/2015JB012595

[74] Nishenko, S.P., Buland, R., 1987. A generic recurrence interval distribution for earthquake forecasting. Bulletin of the Seismological Society of America, 77:1382–1399.

[75] Okada, Y., 1992. Internal deformation due to shear and tensile faults in a half-space. Bulletin of the Seismological Society of America 82, 1018–1040.

[76] Pace, B., Visini, F., Peruzza, L., 2016. FiSH: MATLAB Tools to Turn Fault Data into Seismic-Hazard Models. Seismological Research Letters 87, 374–386. https://doi.org/10.1785/0220150189

[77] Pagani, M., Monelli, D., Weatherill, G.A. and Garcia, J., 2014. The OpenQuake-engine Book: Hazard. Global Earthquake Model (GEM) Technical Report 2014-08, doi: 10.13117/-GEM.OPENQUAKE.TR2014.08, 67pp.

[78] Page, M.T., Field, E.H., Milner, K.R., Powers, P.M., 2014. The UCERF3 Grand Inversion: Solving for the Long-Term Rate of Ruptures in a Fault System. Bulletin of the Seismological Society of America 104, 1181–1204. https://doi.org/10.1785/0120130180

[79] Papadopoulos, A.N., Bazzurro, P., Marzocchi, W., 2020. Exploring probabilistic seismic risk assessment accounting for seismicity clustering and damage accumulation: Part I. Hazard analysis: Earthquake Spectra. https://doi.org/10.1177/8755293020957338

[80] Parsons, T., 2000. Heightened Odds of Large Earthquakes Near Istanbul: An Interaction-Based Probability Calculation. Science 288, 661–665. https://doi.org/10.1126/science.288.5466.661

[81] Parsons, T., 2004. Recalculated probability of $M \geq 7$ earthquakes beneath the Sea of Marmara, Turkey: probability of earthquakes beneath Marmara Sea. Journal of Geophysical Research: Solid Earth 109. https://doi.org/10.1029/2003JB002667

[82] Parsons, T., 2005. Significance of stress transfer in time-dependent earthquake probability calculations. Journal of Geophysical Research: Solid Earth 110, B05S02. https://doi.org/10.1029/2004JB003190

[83] Parsons, T., 2008. Monte Carlo method for determining earthquake recurrence parameters from short paleoseismic catalogs: Example calculations for California. Journal of Geophysical Research: Solid Earth 113, B03302. https://doi.org/10.1029/2007JB004998

[84] Parsons, T., 2012. Paleoseismic interevent times interpreted for an unsegmented earthquake rupture forecast. Geophysical Research Letters. 39, L13302. https://doi.org/10.1029/2012GL052275

[85] Parsons, T., Field, E.H., Page, M.T., Milner, K., 2012. Possible Earthquake Rupture Connections on Mapped California Faults Ranked by Calculated Coulomb Linking Stresses. Bulletin of the Seismological Society of America 102, 2667–2676. https://doi.org/10.1785/0120110349

[86] Parsons, T., Geist, E.L., 2009. Is There a Basis for Preferring Characteristic Earthquakes over a Gutenberg-Richter Distribution in Probabilistic Earthquake Forecasting? Bulletin of the Seismological Society of America 99, 2012–2019. https://doi.org/10.1785/0120080069

[87] Petersen, M.D., Cao, T., Campbell, K.W., Frankel, A.D., 2007. Time-independent and Time-dependent Seismic Hazard Assessment for the State of California: Uniform California Earthquake Rupture Forecast Model 1.0. Seismological Research Letters 78, 99–109. https://doi.org/10.1785/gssrl.78.1.99

[88] Pino, N.A., Convertito, V., Madariaga, R., 2019. Clock advance and magnitude limitation through fault interaction: the case of the 2016 central Italy earthquake sequence. Sci Rep 9, 5005. https://doi.org/10.1038/s41598-019-41453-1

[89] Polidoro, B., Iervolino, I., Chioccarelli, E., Giorgio, M., 2013. Models and issues in time-dependent mainshock hazard. ICOSSAR, 11th International Conference on Structural Safety & Reliability 16-20 June, Columbia University, New York.

[90] Reid H.F., 1910. The mechanics of the earthquakes, vol. 2 of the California Earthquake of April 18 1906. Report of the State Earthquake Investigation Commission. Carnegie Institution of Washington Publication 87

[91] Rhoades, D.A., Stirling, M.W., Schweig, E.S., Van Dissen, R.J. 2004. Time-varying earthquake hazard in the Wellington region. Institute of Geological & Nuclear Sciences client report 2004/141, 46p

[92] Rhoades, D.A., Van Dissen, R.J., Langridge, R.M., Little, T.A., Ninis, D., Smith, E.G.C., Robinson, R., 2011. Re-evaluation of conditional probability of rupture of the Wellington-Hutt Valley segment of the Wellington Fault. Bulletin of New Zealand Society for Earthquake Engineering 44, 77–86. https://doi.org/10.5459/bnzsee.44.2.77-86

[93] Rodgers, D.W., Little, T.A., 2006. World's largest coseismic strike-slip offset: The 1855 rupture of the Wairarapa Fault, New Zealand, and implications for displacement/length scaling of continental earthquakes. Journal of Geophysical Research: Solid Earth 111, B12408. https://doi.org/10.1029/2005JB004065

[94] Saltelli, A., Annoni, P., Azzini, I., Campolongo, F., Ratto, M., Tarantola, S., 2010. Variance based sensitivity analysis of model output. Design and estimator for the total sensitivity index. Computer Physics Communications 181, 259–270. https://doi.org/10.1016/j.cpc.2009.09.018

[95] Schermer, E.R., Little, T.A., Rieser, U., 2009. Quaternary deformation along the Wharekauhau fault system, North Island, New Zealand: Implications for an unstable linkage between active strike-slip and thrust faults. Tectonics 28, TC6008. https://doi.org/10.1029/2008TC002426

[96] Schwartz, D.P., Coppersmith, K.J., 1984. Fault behavior and characteristic earthquakes: Examples from the Wasatch and San Andreas Fault Zones. Journal of Geophysical Research: Solid Earth 89, 5681–5698. https://doi.org/10.1029/JB089iB07p05681

[97] Schwartz, D.P., Haeussler, P.J., Seitz, G.G., Dawson, T.E., 2012. Why the 2002 Denali fault rupture propagated onto the Totschunda fault: Implications for fault branching and seismic hazards. Journal of Geophysical Research: Solid Earth 117. https://doi.org/10.1029/2011JB008918

[98] Shaw, B.E., 2013. Appendix E: Evaluation of magnitude-scaling relationships and depth of rupture: Recommendation for UCERF3, U.S. Geological Survey Open-File Report 2013-1165-E, and California Geol. Surv. Special Rept. 228-E.

[99] Stafford, P.J., Strasser, F.O., Bommer, J.J., 2008. An evaluation of the applicability of the NGA models to ground-motion prediction in the Euro-Mediterranean region. Bull Earthquake Eng 6, 149–177. https://doi.org/10.1007/s10518-007-9053-2

[100] Stein, R.S., 1999. The role of stress transfer in earthquake occurrence. Nature 402, 605–609. https://doi.org/10.1038/45144

[101] Stein, R.S., Barka, A.A., Dieterich, J.H., 1997. Progressive failure on the North Anatolian fault since 1939 by earthquake stress triggering. Geophysical Journal International 128, 594–604. https://doi.org/10.1111/j.1365-246X.1997.tb05321.x

[102] Stein, S., Geller, R.J., Liu, M., 2013. Reply to comment by Arthur Frankel on "Why Earthquake Hazard Maps Often Fail and What to do About It." Tectonophysics 592, 207–209. https://doi.org/10.1016/j.tecto.2013.01.024

[103] Stirling, M., McVerry, G., Gerstenberger, M., Litchfield, N., Van Dissen, R., Berryman, K., Barnes, P., Wallace, L., Villamor, P., Langridge, R., Lamarche, G., Nodder, S., Reyners, M., Bradley, B., Rhoades, D., Smith, W., Nicol, A., Pettinga, J., Clark, K., Jacobs, K., 2012. National Seismic Hazard Model for New Zealand: 2010 Update. Bulletin of the Seismological Society of America 102, 1514–1542. https://doi.org/10.1785/0120110170

[104] Toda, S., Stein, R.S., Sevilgen, V., Lin, J., 2011. Coulomb 3.3 Graphic-rich deformation and stress-change software for earthquake, tectonic, and volcano research and teaching – user guide, U.S. Geological Survey Open-File Report 2011-1060, pp 63, available at http://pubs.usgs.gov/of/2011/1060

[105] Toda, S., Stein, R.S., Reasenberg, P.A., Dieterich, J.H., Yoshida, A., 1998. Stress transferred by the 1995 Mw = 6.9 Kobe, Japan, shock: Effect on aftershocks and future earthquake probabilities. Journal of Geophysical Research: Solid Earth 103, 24543–24565. https://doi.org/10.1029/98JB00765

[106] Toda, S., Stein, R.S., 2020. Long- and Short-Term Stress Interaction of the 2019 Ridgecrest Sequence and Coulomb-Based Earthquake Forecasts. Bulletin of the Seismological Society of America. https://doi.org/10.1785/0120200169

[107] Tullis, T.E., 2012. Preface to the Focused Issue on Earthquake Simulators. Seismological Research Letters 83, 957–958. https://doi.org/10.1785/0220120122

[108] Valentini, A., DuRoss, C.B., Field, E.H., Gold, R.D., Briggs, R.W., Visini, F., Pace, B., 2020. Relaxing Segmentation on the Wasatch Fault Zone: Impact on Seismic Hazard. Bulletin of the Seismological Society of America 110, 83–109. https://doi.org/10.1785/0120190088

[109] Valentini, A., Pace, B., Boncio, P., Visini, F., Pagliaroli, A., Pergalani, F., 2019. Definition of Seismic Input From Fault-Based PSHA: Remarks After the 2016 Central Italy Earthquake Sequence. Tectonics 38, 595–620. https://doi.org/10.1029/2018TC005086

[110] Van Dissen, R., Rhoades, D., Little, T., Litchfield, N., Carne, R., Villamor, P., 2013. Conditional probability of rupture of the Wairarapa and Ōhariu faults, New Zealand. New Zealand Journal of Geology and Geophysics 56, 53–67. https://doi.org/10.1080/00288306.2012.756042

[111] Verdecchia, A., Carena, S., Pace, B., DuRoss, C.B., 2019. The effect of stress changes on time-dependent earthquake probabilities for the central Wasatch fault zone, Utah, USA. Geophysical Journal International 219, 1065–1081. https://doi.org/10.1093/gji/ggz336

[112] Verdecchia, A., Pace, B., Visini, F., Scotti, O., Peruzza, L., Benedetti, L., 2018. The Role of Viscoelastic Stress Transfer in Long-Term Earthquake Cascades: Insights After the Central Italy 2016-2017 Seismic Sequence. Tectonics 37, 3411–3428. https://doi.org/10.1029/2018TC005110

[113] Villani, F., Civico, R., Pucci, S., Pizzimenti, L., Nappi, R., De Martini, P.M., 2018. A database of the coseismic effects following the 30 October 2016 Norcia earthquake in Central Italy. Scientific Data 5, 180049. https://doi.org/10.1038/sdata.2018.49

[114] Visini, F., Pace, B., 2014. Insights on a Key Parameter of Earthquake Forecasting, the Coefficient of Variation of the Recurrence Time, Using a Simple Earthquake Simulator. Seismological Research Letters 85, 703–713. https://doi.org/10.1785/0220130165

[115] Visini, F., Valentini, A., Chartier, T., Scotti, O., Pace, B., 2020. Computational Tools for Relaxing the Fault Segmentation in Probabilistic Seismic Hazard Modelling in Complex Fault Systems. Pure and Applied Geophysics. 177, 1855–1877. https://doi.org/10.1007/s00024-019-02114-6

[116] Wang, K., Dreger, D.S., Tinti, E., Bürgmann, R., Taira, T., 2020. Rupture Process of the 2019 Ridgecrest, California Mw 6.4 Foreshock and Mw 7.1 Earthquake Constrained by Seismic and Geodetic Data. Bulletin of the Seismological Society of America. https://doi.org/10.1785/0120200108

[117] Weatherill, G.A., Silva, V., Crowley, H., Bazzurro, P., 2015. Exploring the impact of spatial correlations and uncertainties for portfolio analysis in probabilistic seismic loss estimation. Bulletin Earthquake Engineering 13, 957–981. https://doi.org/10.1007/s10518-015-9730-5

[118] Weldon, R.J., II, Biasi G.P., 2013. Appendix I: Probability of detection of ground rupture at paleoseismic sites, U.S. Geological Survey Open-File Report 2013-1165-I, and California Geol. Surv. Special Rept. 228-I

[119] Wells, D.L., Coppersmith, K.J., 1994. New empirical relationships among magnitude, rupture length, rupture width, rupture area, and surface displacement. Bulletin of the Seismological Society of America 84, 974–1002.

[120] Wesnousky, S.G., 2006. Predicting the endpoints of earthquake ruptures. Nature 444, 358–360. https://doi.org/10.1038/nature05275

[121] Wesnousky, S.G., Scholz, C.H., Shimazaki, K., Matsuda, T., 1983. Earthquake frequency distribution and the mechanics of faulting. Journal of Geophysical Research: Solid Earth 88, 9331–9340. https://doi.org/10.1029/JB088iB11p09331

[122] Working Group on California Earthquake Probabilities (WGCEP), 2003. Earthquake Probabilities in the San Francisco Bay Region: 2002–2031, U.S. Geological Survey Open-File Report 03-214

[123] Working Group on California Earthquake Probabilities (WGCEP), 1990. Probabilities of large earthquakes in the San Francisco Bay region, California, U.S. Geological Survey Open-File Report, 1053, 51 pp.

[124] Youngs, R.R., Arabasz, W.J., Anderson, R.E., Ramelli, A.R., Ake, J.P., Slemmons, D.B., McCalpin, J.P., Doser, D.I., Fridrich, C.J., Swan, F.H., Rogers, A.M., Yount, J.C., Anderson, L.W., Smith, K.D., Bruhn, R.L., Knuepfer, P.L.K., Smith, R.B., dePolo, C.M., O'Leary, D.W., Coppersmith, K.J., Pezzopane, S.K., Schwartz, D.P., Whitney, J.W., Olig, S.S., Toro, G.R., 2003. A Methodology for Probabilistic Fault Displacement Hazard Analysis (PFDHA). Earthquake Spectra 19, 191–219. https://doi.org/10.1193/1.1542891

[125] Zhuang, J., Werner, M.J., Zhou, S., Harte, D., Hainzl, S., 2011. Basic models of seismicity: spatiotemporal models. https://doi.org/10.5078/CORSSA-07487583

Appendix A – Inversion constraints

A.1. Slip rates balancing equation-set

This constraint enforces the fact that the average slip D_{sr} in each rupture r that includes a given fault subsection s, multiplied by the rate f_r of that rupture, must sum to the long-term slip rate v_s for that subsection (Page et al. 2014 and Field and Page 2011). This constraint is applied to each fault subsection in both normalized and unnormalized form, as written below:

$$\sum_{r=1}^{R} D_{sr} f_r = v_s \quad \text{and} \quad \sum_{r=1}^{R} \frac{D_{sr} f_r}{v_s'} = \frac{v_s}{v_s'} \tag{A 1}$$

where R is the number of ruptures. For the normalized constraint, each slip rate constraint equation is normalized by the target slip rate $v_s' = \max\,(0.1\ mm/yr, v_s)$. Including both normalized and unnormalized forms of this constraint means that both the ratio and the difference between the target and model slip rates are minimized. The target slip rates are bounded to 0.1 mm/yr to avoid extremely low slip rates dominating the calculated misfit during the optimization process.

To establish these equations, the average slip on the s^{th} subsection in the r^{th} rupture, D_{sr} is needed, where the word "average" indicates that this value is the average over multiple occurrences of the event. The simplest way to compute D_{sr} is to first compute the average slip for a given rupture D_r and then partition this among the subsections to get D_{sr}. D_r is computed converting the magnitude of the rupture to the related seismic moment M_{0r} and then dividing by the rupture area A_r of the rupture and shear modulus G (assumed equal to $3.0 \cdot 10^{10}\ Pa$):

$$D_r = \frac{M_{0r}}{GA_r} = \frac{10^{1.5 M_{W,r} + 9.05}}{GA_r} \tag{A 2}$$

where the area of the rupture A_r is the sum of associated subsections and the magnitude $M_{W,r}$ of each rupture can be computed from a magnitude-area scaling relations such as Wells and Coppersmith (1994) or others. Alternative methods to obtain D_r and alternative magnitude-area scaling relations can be easily integrated in the framework if considered to be more appropriate for the region under analysis (e.g., Shaw 2013; Hanks and Bakun 2008).

Once D_r is computed, it needs to be spread among the subsections composing the rupture to get D_{sr} using the shape of the average single-event slip. The tapered-slip model has empirical basis and has a square-root-sine functional form of the normalized length (Biasi et al. 2013):

$$D_{sr}(l) = 1.311 D_r [\sin\,(\pi l/L)]^{1/2} \tag{A 3}$$

where L is the entire rupture length and l is in the range $0 \le l \le L$. The constant factor 1.311 is one divided by the average of the $[(sin(\pi x)]^{1/2}$ term. This model assumes that intra-event, along-strike slip variability averages out over multiple occurrences to yield the tapered shape. Alternative slip models (e.g., the uniform distribution of the slip along the strike, Field et al. 2014) can be easily incorporated in the framework.

A.2. Paleoseismic event rate matching equation-set

This equation-set uses data from paleoseismic trench studies to constrain the rupture rates. Since not all ruptures that occurred beneath a site are paleoseismicially observable, the detection probability factor P_r^{paleo} is used to specify the probability that the r^{th} rupture would be seen in a trench study (Page et al. 2014).

$$\sum_{r=1}^{R} \frac{G_{sr} P_{sr}^{paleo}}{\sigma_s} f_r = \frac{f_s^{paleo}}{\sigma_s} \quad \text{(A 4)}$$

where $G_{sr} = 1$ if the r^{th} rupture includes the s^{th} subsection and 0 otherwise, P_r^{paleo} gives the probability that the r^{th} rupture will be observed at the s^{th} subsection, f_s^{paleo} is the paleoseismically observed mean event rate for the s^{th} subsection, and σ_s is the standard deviation of the mean observed event rate. The equation above means that the total rate of all ruptures that include a given fault subsection, multiplied by the detection probability each rupture is paleoseismically visible, must sum to the mean paleoseismic event rate for that subsection.

The compilation of event dates for various paleoseismic studies is needed for the available fault subsections. The estimates of the mean peleoseismic event rates (along with the standard deviation of the mean observed event rate) can be computed from these past events dates with several methods (Biasi et al. 2002, Biasi et al. 2015, Pace et al. 2016) and one of the occurrence models mentioned in Section 2.2. The Biasi et al. (2015) and the BPT distribution (Ellsworth et al. 1999 and Matthews et al. 2002) are used in this study. The Biasi et al. (2015) method creates sample earthquake sequences by drawing from each event probability distribution independently to estimate occurrence model parameters. Since event date distributions can overlap, samples not respecting the events' actual order (e.g., event 2 is reported to occur before event 1) are discarded. An additional geologically motivated constraint is imposed: the minimum separation time between events cannot be lower than 20 years. An adaptation of the Maximum Likelihood approach (Ellsworth et al. 1999) is than applied to compute the most probable occurrence model parameters and the corresponding confidence intervals. The method proposed by Biasi et al. (2015) is also able to account for the open interval from the most recent event occurred in the considered site.

The simple model used in the proposed methodology for calculating the probabilities of seeing a given rupture in a trench P_r^{paleo} is the one proposed by Youngs et al. (2003):

$$P_r^{paleo} = \frac{e^{2.053M_W - 12.51}}{1 + e^{2.053M_W - 12.51}} \quad \text{(A 5)}$$

where M_W is the moment magnitude of the event.

Another (more advanced) model is given by Weldon and Biasi (2013). This model depends on both:

- the average slip of the rupture D_r: the higher D_r of the past event, the higher the probability of detecting that event; and
- the position of the site relative to the nearest end of the rupture, implying that it is less likely to observe surface offsets near the ends of a rupture (which is consistent with the square-root-sine functional form of the D_r mentioned in the previous section)

However, the model proposed by Weldon and Biasi (2013) was calibrated based on only one site in California and its applicability to more general cases should be further investigated.

A.3. Fault segment smoothness constraint equation-set

In satisfying the above paleoseismic event rates, there is the risk that the inversion would simply put a high (or low) rate of events right at the paleoseismic sites. The smoothness constraint equation-set helps mitigate this behavior by providing an along-fault smoothing constraint that minimizes curvature in the events' along-fault rate (Page et al. 2014 and Field and Page 2011).

The Laplacian smoothing formula proposed by Page et al. (2014) is used. This formula constraints the rate of events nucleating in a given magnitude bin to vary smoothly along strike. For each subsection s on a fault with paleoseismic data and its adjacent subsections $s-1$ and $s+1$:

$$(R_s^m - R_{s-1}^m) + (R_s^m - R_{s+1}^m) = 0 \qquad \text{(A 6)}$$

where R_s^m is the nucleation rate of events in the m^{th} magnitude bin on the s^{th} subsection. Note that this constraint is only applied to fault segments with one or more paleoseismic event-rate constraints and not beyond the ends of fault segments.

A.4. Improbability constraint equation-set

The improbability constraints can force a lower rate on any designated event or event type, such as multi-segment ruptures or floating ruptures. There are studies in the literature (e.g., Valentini et al. 2020) that try to theoretically or empirically support/guide the assignment of improbability constraints. This constraint was not used in UCERF3, because it was deemed to be redundant. Valentini et al. (2020) showed how this constraint can be used to force multi-segment ruptures never to occur. Defining s' and s'' as the subsections adjacent to the a priori segmentation boundary, any ruptures that overcome the boundary can be penalized as follows:

$$f_r = 0 \text{ if } G_{s'r} = G_{s''r} = 1 \qquad \text{(A 7)}$$

It is also possible to penalize the floating ruptures. Given n_r as the number of subsections in the r^{th} rupture and n_{seg} the total number of subsections in the fault segment, the floating ruptures can be forced to never occur as follows:

$$f_r = 0 \text{ if } n_r \neq n_{seg} \qquad \text{(A 8)}$$

A.5. Fault segment MFD constraint equation-set

This constraint adds the possibility to force the MFD of the fault segment to be as close as possible to a chosen shape. The constraints equations are written as:

$$\sum_{r=1}^{R} \frac{M_{sr}^m}{R_s^m} f_r = 1 \ \text{ for all } \ R_s^m > 0 \qquad \text{(A 9)}$$

where M_{sr}^m is the fraction of the r^{th} rupture of events in the m^{th} magnitude bin on the s^{th} subsection. Rupture rates for magnitude bins where $R_s^m = 0$ are also minimized.

A.6. Minimum rate constraint

This constraint can be used to guarantee that the rupture rates f_r are not below an imposed f_{min} is the minimum rupture rate:

$$f_r \geq f_{min} \qquad \text{(A 10)}$$

Since the rupture rates cannot be negative by definition, the minimum f_{min} is zero, but there might be reasons to choose a higher number (Page et al. 2014 and Field and Page 2011). This constraint is not included in the equation system but is enforced directly in the solving algorithm (Page et al. 2014), which does not search any solution space that contains negative rates.

Appendix B – Details of the time-dependent probabilities

This appendix provides details of the time-dependent probability calculations used in the proposed framework. First, the Brownian Passage Time (BPT) occurrence model is explained, with a focus on the key parameters. The methodology proposed by Field (2015) to compute the time-dependent probability knowing the time elapsed since the last event is then introduced. Finally, the treatment of the unknown time since the last event by Field and Jordan (2015) and Field et al. (2015) is presented.

B.1. BPT model

The most used "elastic rebound" motivated earthquake occurrence model is the BPT model (see Section 2.2), proposed by Ellsworth et al. (1999) and Matthews et al. (2002). The BPT functional form is an inverse Gaussian distribution, characterized by only two parameters: the mean recurrence time (μ) between events and the aperiodicity (α) of the mean recurrence time, which is equivalent to the coefficient of variation ($\alpha = CoV$). The probability density function (PDF) of the BPT model is:

$$f(t) = \sqrt{\frac{\mu}{2\pi\alpha^2\tau^3}} exp\left(-\frac{(t-\mu)^2}{2\mu\alpha^2 t}\right) \qquad \text{(B 1)}$$

where t is the interarrival time between two subsequent events. The mean recurrence time between events (μ) is the scale parameter in the BPT formulation, which rescales the distribution in time. The aperiodicity (α) is the shape parameter (i.e., it modifies the shape of the distribution) and it represents a dimensionless measure of the irregularity in the event sequence. A perfectly periodic sequence has an $\alpha = CoV = 0$, while the BPT tends to a random (i.e., Poissonian) process as the α (CoV) increases.

With a renewal time-dependent occurrence model, the conditional earthquake occurrence probabilities depend on the following parameters:

- the time since the last event (T_e);
- the forecast duration (ΔT); and
- the BPT parameters: the mean recurrence interval (μ) and the aperiodicity (α).

However, the normalized values of the above variables are more useful to describe the rebound phenomenon (Field 2015): the normalized time since last event (T_e/μ) and the normalized duration ($\Delta T/\mu$). These represent the extent of T_e and ΔT relative to the mean recurrence interval.

B.2. Time-dependent probabilities

Knowing the long-term rates f_r of each rupture r from the inversion step (Section 3.2), the rate of events f_s on each subsection s can be simply computed as the summation of rates f_r of the ruptures containing the s^{th} subsection:

$$f_s = \sum_{r=1}^{R} G_{sr} f_r \qquad \text{(B 2)}$$

where G_{sr} is a boolean matrix (ones and zeros) containing all the subsections utilized by the generated ruptures. The corresponding mean recurrence interval of each subsection μ_s can be computed as the inverse of the relative rate:

$$\mu_s = 1/f_s \qquad \text{(B 3)}$$

If the r^{th} rupture is assumed to be the next to occur, its expected recurrence interval can be computed as a weighted average over the long-term recurrence intervals μ_s of each subsection involved:

$$\mu_r^{next} = \frac{\sum \mu_s A_s}{\sum A_s} \quad \text{(B 4)}$$

where, A_s is the subsection area, and the sums are over all the subsections included in the r^{th} rupture. The "next" superscript refers to the fact that the expected recurrence interval is computed assuming the r^{th} rupture will be the next event to occur. The use of subsection area as weights is consistent with the elastic-rebound-based simulations presented by Field (2015).

As a proxy for how close the rupture is to failure, the average normalized time since the last event for each rupture will be used:

$$\eta_r = \frac{\sum (T_e/\mu_s) A_s}{\sum A_s} \quad \text{(B 5)}$$

where T_e is the time since the last event on the s^{th} subsection and the sums are only over the subsections utilized by the r^{th} rupture.

From the average normalized time since the last event (η_r), the normalized forecast duration ($\Delta T/\mu_r^{next}$), and an assumed aperiodicity (α), it is possible to compute the conditional probability of occurrence for the rupture using a renewal model and:

$$P_r^{BPT} = P(T \leq t \leq T + \Delta T \mid t > T) = \frac{\int_T^{T+\Delta T} f(t)dt}{\int_T^{\infty} f(t)dt} \quad \text{(B 6)}$$

In the context of this paper, the BPT renewal model, Equation (B 1), is used to compute conditional rupture probabilities but any time-dependent occurrence model can be used. This probability is calculated assuming that the r^{th} will be the next to occur and is conditional to the knowledge of the time elapsed since the last event. To account for the fact that the next occurring rupture (amongst the many overlapping ones) is unknown, the conditional probability of occurrence above is then multiplied by the ratio of the conditional rupture recurrence interval to the long-term recurrence interval (μ_r^{next}/μ_r). This is used as a proxy for probability that the r^{th} rupture is chosen (i.e., it is the likelihood of selecting the r^{th} rupture given an occurrence of one the overlapping possibilities). Thus, the total conditional probability of occurrence of each rupture can be computed as:

$$P_r = P_r^{BPT} \left[\frac{\mu_r^{next}}{\mu_r} \right] \quad \text{(B 7)}$$

One advantage of this method is the ability to apply magnitude-dependent aperiodicity. Table B 1 lists three sets of magnitude-dependent aperiodicity values inferred from physics-based simulations by Field (2015).

Table B 1. Sets of magnitude-dependent aperiodicity values based on physics-based simulations (after Field 2015).

	Aperiodicity			
Recurrence uncertainty	**$M_W \leq 6.7$**	**$6.7 < M_W \leq 7.2$**	**$7.2 < M_W \leq 7.7$**	**$M_W > 7.7$**
Low	0.4	0.3	0.2	0.1
Mid	0.5	0.4	0.3	0.2
High	0.6	0.5	0.4	0.3

B.3. Unknown time since the last event

The computation of the conditional probability of rupture occurrence discussed so far assumes the knowledge of the last event's date, which is not available in most cases. For faults where this date is unknown, the usual approach is to use a time-independent Poisson model to obtain earthquake probabilities. Field and Jordan (2015) investigated this issue and proposed a formulation to compute the conditional probability of having an event in a certain forecast duration (ΔT) and accounting for the fact that the time elapsed is known to be constrained by the "historic open interval" (T_H):

$$P_r^{BPT} = \frac{\Delta T - \int_{T_H}^{T_H+\Delta T} F(T)dT}{\int_{T_H}^{\infty}[1 - F(T)]dT} \tag{B 8}$$

where $F(T)$ is the cumulative distribution function (CDF) of the interarrival time between events for a given renewal occurrence model (e.g., BPT distribution). The historic open interval can be inferred from the historical earthquakes catalogue: if there is no record of an event occurred on the fault segment of interest in the earthquake catalogue, the completeness period can be used as the historic open interval.

Field et al. (2015) suggested an approximate method to treat those ruptures where the last event's date is known on some subsections but not others. The conditional probability of occurrence of the rupture, P_r^{BPT}, can be computed as:

$$P_r^{BPT} = \int_{T_H/\mu^u}^{\infty} p(\eta^u \mid \eta^u \geq T_H/\mu^u)\, P^{BPT}(\eta_r, \Delta T/\mu_r) d\eta^u \tag{B 9}$$

where μ^u is the average recurrence interval where the time since the last event is unknown, η^u is the average normalized time since the last event where unknown, $P^{BPT}\left(\eta_r, \Delta T/\mu_r\right)$ is computed with Equation (B 6), μ_r is the long-term recurrence interval of the rupture and η_r is the normalized time since the last event for the rupture, computed as:

$$\eta_r = \frac{A^u\eta^u + A^k\eta^k}{A^u + A^k} \tag{B 10}$$

where η^k is the average normalized time since the last event where known and A^u and A^k are the sums of the areas of the subsections where the time since the last event is unknown and known, respectively. The probability of having a normalized time since the last event η^u given that the interarrival time between events has to be greater than the open historical time interval is:

$$p(\eta^u \mid \eta^u \geq T_H/\mu^u) = \frac{1 - F(t)}{\int_{T_H/\mu^u}^{\infty}[1 - F(\tau)]d\tau} \tag{B 11}$$

Appendix C – Fault interaction details

C.1. Coulomb stress transfer

Since direct measurements of induced stress changes are not possible, slipping a dislocation in an elastic half-space with uniform isotropic elastic properties is used to estimate the static change in the stress field (Okada 1992). Changed stress tensor components are resolved on planes of interest (i.e., known fault planes) and related to triggering or inhibition of future earthquakes. The Coulomb failure stress change (ΔCFF) can be written as:

$$\Delta CFF = \Delta\tau + FC\ \Delta\sigma_n \tag{C 1}$$

where $\Delta\tau$ is the shear stress change in the slip direction, $\Delta\sigma_n$ the normal stress change and FC is the effective coefficient of friction (Toda et al. 2011). The effective coefficient of friction usually varies between 0 and 0.75, with an average value of 0.4 that is widely used in Coulomb stress modeling studies for major faults (King et al. 1994). Failure is promoted if $\Delta CFF > 0$ and inhibited if $\Delta CFF < 0$ (Parsons 2005, Toda and Stein 2020).

For this study, the computation of the Coulomb static stress changes for each subsection s (ΔCFF_s) is carried out with the software Coulomb v3.3 (Toda et al. 2011), which was extensively tested and used in the literature (e.g., Murru et al. 2016, Mignan et al. 2016). The calculation is done imposing a "source rupture", where a coseismic slip is assumed to be known, and computing the ΔCFF_s on the "receiver subsections", where strike, dip, and rake must be known. Typical inputs needed for Coulomb v3.3 are:

- the geometries (including strike, dip, and rake) of the rupture source and the nearby (receiver) subsection planes. Each subsection is discretized in smaller patches of about 3km x 3km, which are fed to Coulomb v3.3;
- Poisson's ratio, a value of 0.25 is typically used (Toda et al. 2011);
- Young's modulus, $8 \cdot 10^5$ bars is typically used (Toda et al. 2011);
- Effective friction coefficient, $FC = 0.4$ is often used (King et al. 1994).

An estimate of the slip distribution on the source rupture is also needed, along with the dimensions (width and length) of the surfaces involved (source and receivers). For simplicity, the slip distribution is assumed to be a square-root-sine functional form of the normalized length, also called tapered-slip model (Biasi et al. 2013, Murru et al. 2016). More complicated distributions are possible if the hypocenter is also randomly sampled during the simulations (Goda et al. 2017).

C.2. Coulomb stress change effects

Both the permanent and the transient effects of the Coulomb stress changes are included. Two very similar methods have been proposed in the literature to estimate the permanent effect of a stress change on the conditional probability of rupture occurrence. The first method advances the elapsed time (for each subsection s) in the conditional probability calculation from T_e to T_e' (i.e., clock change) by the equivalent time required to accumulate the stress step through the tectonic stressing process (Dieterich 1988, Toda et al. 1998, Murru et al. 2016):

$$T_e' = T_e + \frac{\Delta CFF_s}{\dot{\tau}_s} \tag{C 2}$$

where $\dot{\tau}_s$ is the tectonic stressing rate computed on the s^{th} subsection. The second approach reduces the expected mean recurrence time from μ_s' to μ_s (for each subsection s) by the equivalent time required to accumulate the stress step through the tectonic stressing process (WGCEP 1990, Mignan et al. 2016):

$$\mu_s' = \mu_s - \frac{\Delta CFF_s}{\dot{\tau}_s} \tag{C 3}$$

Reducing μ_s or increasing T_e for a positive step in stress increases the conditional probability of an earthquake. The choice of whether to change the elapsed time or the mean recurrence time has a different effect on the resulting earthquake probability calculation (Stein et al. 1997, Parsons 2005). Probability calculated with a clock change is most significant at the time of the stress change, and then tends to the maximum probability value with time. A change in mean recurrence interval has the opposite characteristic: the probability change is smallest at the time of the stress change and tends to a lower probability (with a permanent offset). This difference arises from the fact that changing the mean recurrence time, changes the earthquake occurrence distribution permanently, while changing the time elapsed since the last event does not change the occurrence distribution. There is no empirical evidence to support one model against the other (Parsons 2005). Thus, in the proposed methodology, the Equation (C 2) is used (i.e., modifying the time elapsed since the last event of each subsection) because it is simpler to implement in the framework and it does not change the calibrated time-dependent mean recurrence time of the ruptures. If the time since the last event is unknown, the open historic interval T_H is instead increased to emulate a positive clock change (promoting failure) or decreased to emulate a negative clock change (inhibiting failure). For the r^{th} rupture, the open historic interval change $\Delta T_{H,r}$ is calculated as:

$$\Delta T_{H,r} = \frac{\sum(\Delta CFF_s/\dot{\tau}_s)A_s}{\sum A_s} \tag{C 4}$$

where A_s is the subsection area, and the sums are over all the subsections included in the r^{th} rupture where the time elapsed since the last event is unknown. This approach is consistent with the findings and the methodologies presented by Field (2015).

The transient effect of the stress change is here quantified with the state-dependent formulation proposed by Dieterich (1994) as implemented by Toda et al. (1998) and Mignan et al. (2016). The new conditional probability of occurrence of the r^{th} rupture including the transient effects ($P_{new,r}$) is expressed through a non-stationary Poisson process as

$$P_{new,r} = 1 - \exp\left(-N_r\right) \tag{C 5}$$

where N_r is the expected number of times the r^{th} rupture occurs during a given time interval $[t_0, t_1]$ after a stress-inducing earthquake occurred at time t_{last}. Following Toda et al. (1998), N_r can be calculated as

$$\begin{aligned} N_r &= r_p^c(t_1 - t_0) \\ &+ r_p^1 t_a \log\left[\frac{1 + \left(\exp\left(-\frac{\Delta CFF_r}{A\sigma}\right) - 1\right)\exp\left(-\frac{(t_1 - t_{last})}{t_a}\right)}{\exp\left(-\frac{\Delta CFF}{A\sigma}\right)}\right] \\ &- r_p^0 t_a \log\left[\frac{1 + \left(\exp\left(-\frac{\Delta CFF_r}{A\sigma}\right) - 1\right)\exp\left(-\frac{(t_0 - t_{last})}{t_a}\right)}{\exp\left(-\frac{\Delta CFF_r}{A\sigma}\right)}\right] \end{aligned} \tag{C 6}$$

where t_a is the aftershock duration, ΔCFF_r is calculated as $\sum \Delta CFF_s\, A_s / \sum A_s$ (sums over all the subsections included in the r^{th} rupture), $A\sigma$ is a parameter of the state-dependent formulation, r_p^c, r_p^1 and r_p^0 are rates calculated as

$$\begin{aligned} r_p^c &= -1/(t_1 - t_0) \cdot \log\left(1 - P_C\right) \\ r_p^1 &= -1/(t_1 - t_{last}) \cdot \log\left(1 - P_1\right) \\ r_p^0 &= -1/(t_0 - t_{last}) \cdot \log\left(1 - P_1\right) \end{aligned} \tag{C 7}$$

where P_C, P_1 and P_0 are conditional probabilities for intervals $[t_0, t_1]$, $[t_{last}, t_1]$ and $[t_{last}, t_0]$, respectively. These are calculated with the methodology described in Appendix B. The global average of the t_a parameter is 10.2 years (Toda et al. 1998, Parsons 2005). Hence, the $t_a = 10yr$ is used in this study. The parameter $A\sigma$ is calculated as $\dot{\tau}_r \cdot t_a$ (Toda et al. 1998), where $\dot{\tau}_r$ is calculated as $\sum \dot{\tau}_s A_s / \sum A_s$ (sums over all the subsections included in the r^{th} rupture). When more than one earthquake has occurred, the total number of expected occurrences N_r in Equation (C 5) is the sum of the individual expected events calculated with Equation (C 6).

An estimate of the tectonic stressing rate $\dot{\tau}_s$ on each subsection is needed to use the clock change adjustment and the transient effects in the probability calculations. A commonly used approach to estimating tectonic loading uses dislocation models or three-dimensional models of the crustal deformation (Parsons 2005). For this study, the tectonic stressing rate of each subsection is estimated from the long-term slip rate V_s (calculated by summing up all the single-event slips of the ruptures, D_{sr} in Section A.1, multiplied by the corresponding long-term rates f_r, Equation (A 1)) and the area of the s^{th} subsection (Murru et al. 2016):

$$\dot{\tau}_s = \frac{32\ \mathrm{G}\ V_s}{\pi^2 \sqrt{A_s}} \qquad \text{(C 8)}$$

where V_s is in meters per year, A_s is the subsection area and G is the average shear modulus of the elastic medium (assumed 30GPa).

Appendix D – Illustrative examples of the proposed framework

Three example cases are used here to illustrate how the conditional probability of rupture occurrence changes when an event (i.e., a rupture) is simulated with the framework illustrated in Figure 4 of the main text. The cases contain up to three ruptures (Rupture 1, Rupture 2, and Rupture 3; described below) and are presented in order of complexity.

D.1. General inputs

The BPT model is used (see Appendix B of the manuscript) as follows:

- Rupture 1: mean recurrence interval $\mu_r^{next} = 200yr$, time elapsed since the last event $T_e = 100yr$ (assumed known on all subsections), aperiodicty $\alpha = 0.4$, $\mu_r^{next}/\mu_r = 0.1$ (where μ_r is the long-term occurrence rate);
- Rupture 2: mean recurrence interval $\mu_r^{next} = 300yr$, time elapsed since the last event $T_e = 150yr$ (assumed known on all subsections), aperiodicty $\alpha = 0.4$, $\mu_r^{next}/\mu_r = 0.1$ (where μ_r is the long-term occurrence rate);
- Rupture 3: imposed (no probability calculations).

The following assumptions are used for the fault interaction calculations (see Appendix C of the manuscript):

- Tectonic stressing rate $\dot{\tau}_r = 0.1$ bars/yr for all ruptures;
- Coulomb stress on the subsections of Rupture 2, when another rupture occurs $\Delta CFF = 1\ bar$ (positive)
- $t_a = 10yr$ ($A\sigma = t_a \cdot \dot{\tau}_r$). References: Toda et al. (1998) and Parsons (2005).

Note that all the following calculations can also be performed when the time elapsed since the last event is unknown for some or all subsections (see Field et al. 2015 and Appendix B).

D.2. Case 1 (Figure D1)

The analysis starts in 2010. Step 3 of the framework (Section 3.3 of the main text) updates the conditional probabilities of rupture occurrence for all ruptures as time elapses. Step 4 of the framework (Section 3.4 of the main text) simulates Rupture 1 at the beginning of January 2030 (see Figure D1). When Rupture 1 occurs, the conditional occurrence probability of Rupture 1 drops to zero (as expected from a time-dependent model), while the conditional probability of occurrence of Rupture 2 increases due to the transient and permanent effects of the Coulomb stress increase (Step 4a Section 3.4.1 of the main text). As time passes, the transient effect decreases to nothing and only the permanent effect remains.

It is worth noting here that the conditional probabilities in Figure D1 are computed on a yearly basis ($w = 1$ in Equation 2 of the main text).

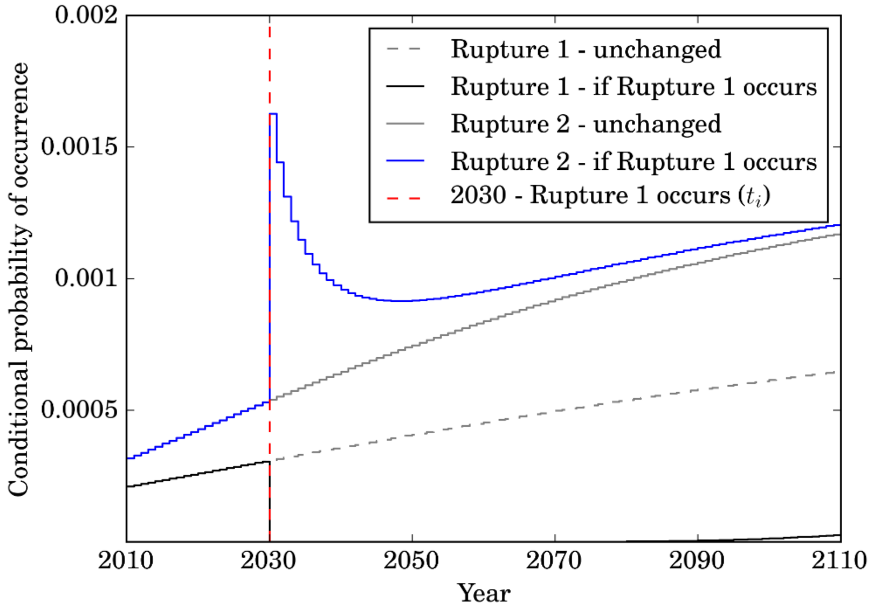

Figure D1. Case 1: conditional probability of rupture occurrence of example Ruptures 1 and 2 with time.

D.3. Case 2 (Figure D2)

Step 4 of the framework (Section 3.4 of the main text) can also be used to compute conditional probabilities of rupture occurrence for post-event time windows less than one year. For this case, it is assumed that Step 4 simulates Rupture 1 at $t_i = 0.08yr$ after the beginning of 2030 (i.e., the end of January 2030; see Figure D1). Step 4 then updates the time window for the calculation of conditional rupture occurrence probability as $w = 1 - t_i$ and the simulation process is repeated. Note that the probabilities of Figure D2 do not correspond exactly to those of Case 1 due to differences in the post-Rupture 1 time window.

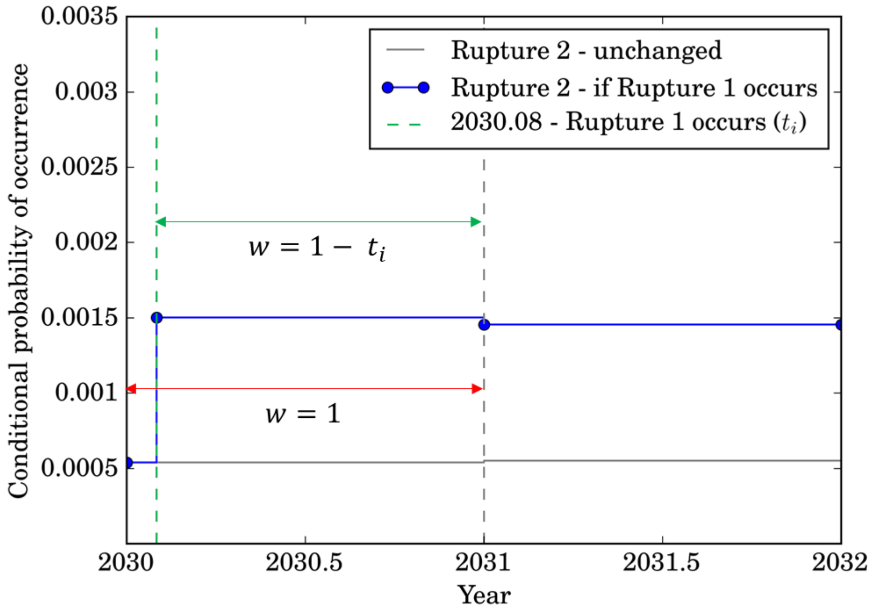

Figure D2. Case 2: conditional probability of rupture occurrence for Rupture 2 between 2030 and 2032. It is assumed that Rupture 1 occurs at the end of January 2030. Note that the x-axis is smaller than that of Figure D1.

D.1. Case 3 (Figure D3)

Step 4 of the framework also enables multiple events to occur within a year. This case assumes Rupture 1 is simulated at $t_{i1} = 0.08yr$ and Rupture 3 is simulated at $t_{i2} = 0.67yr$ after the start of 2030 (i.e., at the end of January and the end of August 2030, respectively). The corresponding conditional occurrence probabilities for Rupture 2 are provided in Figure D3.

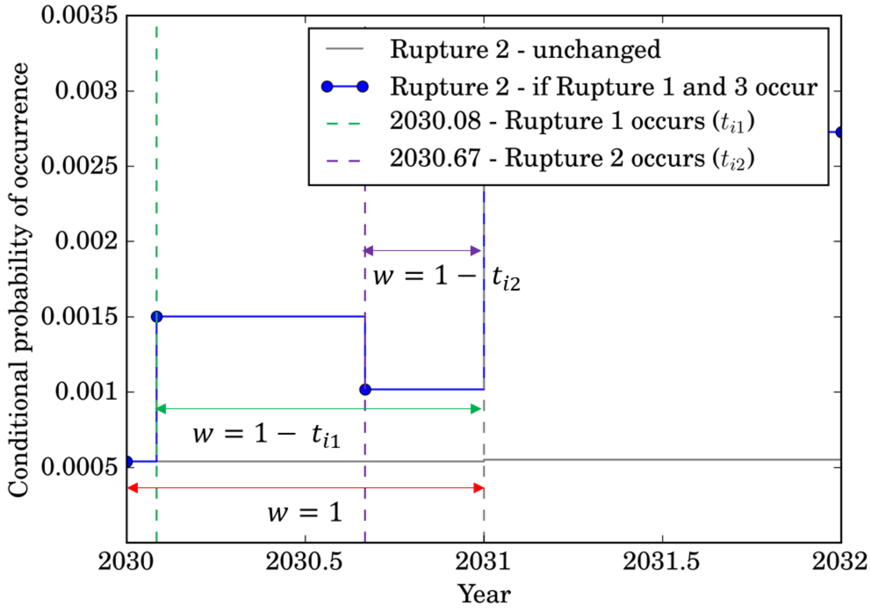

Figure D3. Case 3: conditional probability of rupture occurrence for Rupture 2 between 2030 and 2032. It is assumed that Rupture 1 occurs at the end of January 2030 and Rupture 3 occurs at the end of August 2030.

Note that after the second event (t_{i2}), the probability of rupture occurrence for Rupture 2 decreases because the time window (w) only comprises a few months. At the beginning of 2031, the annual conditional probability of occurrence takes the occurrence of Rupture 1 and 3 (with coulomb stress changes) into account.